Monthly Notices of the ROYAL ASTRONOMICAL SOCIETY
MNRAS **453,** 3729–3753 (2015) doi:10.1093/mnras/stv1662

Beyond Sérsic + exponential disc morphologies in the Coma Cluster

Jacob T. C. G. Head,[1★] John R. Lucey[1★] and Michael J. Hudson[2,3]

[1]*Department of Physics, University of Durham, South Road, Durham DH1 3LE, UK*
[2]*Department of Physics and Astronomy, University of Waterloo, Waterloo, ON N2L 3G1, Canada*
[3]*Perimeter Institute for Theoretical Physics, 31 Caroline St N., Waterloo, ON N2L 2Y5, Canada*

Accepted 2015 July 21. Received 2015 July 12; in original form 2014 November 3

ABSTRACT

Galaxies are not limited to simple spheroid or bulge + disc morphologies. We explore the diversity of internal galaxy structures in the Coma Cluster across a wide range of luminosities ($-17 > M_{\mathrm{g}} > -22$) and cluster-centric radii ($0 < r_{\mathrm{cluster}} < 1.3r_{200}$) through analysis of deep Canada–France–Hawaii Telescope *i*-band imaging. We present 2D multicomponent decomposition via GALFIT, encompassing a wide range of candidate model morphologies with up to three photometric components. Particular focus is placed on early-type galaxies with outer discs (i.e. S0s), and deviations from simple ('unbroken') exponential discs. Rigorous filtering ensures that each model component provides a statistically significant improvement to the goodness-of-fit. The majority of Coma Cluster members in our sample (478 of 631) are reliably fitted by symmetric structural models. Of these, 134 (28 per cent) are single Sérsic objects, 143 (30 per cent) are well-described by 2-component structures, while 201 (42 per cent) require more complex models. Multicomponent Sérsic galaxies resemble compact pseudo-bulges ($n \sim 2$, $R_{\mathrm{e}} \sim 4$ kpc) surrounded by extended Gaussian-like outer structures ($R_{\mathrm{e}} > 10$ kpc). 11 per cent of galaxies ($N = 52$) feature a break in their outer profiles, indicating 'truncated' or 'antitruncated' discs. Beyond the break radius, truncated galaxies are structurally consistent with exponential discs, disfavouring physical truncation as their formation mechanism. Bulge luminosity in antitruncated galaxies correlates strongly with galaxy luminosity, indicating a bulge-enhancing origin for these systems. Both types of broken disc are found overwhelmingly (>70 per cent) in 'barred' galaxies, despite a low measured bar fraction for Coma (20 ± 2 per cent). Thus, galaxy bars play an important role in formation of broken disc structures. No strong variation in galaxy structure is detected with projected cluster-centric radius.

Key words: galaxies: clusters: individual: Abell 1656 – galaxies: elliptical and lenticular, cD – galaxies: evolution – galaxies: formation – galaxies: structure.

1 INTRODUCTION

Lenticular (S0) galaxies occupy the crux of the Hubble sequence, representing the morphological intermediate between disc-dominated spiral galaxies and spheroidal ellipticals. However, it remains unclear whether S0s are *evolutionary* intermediates between star-forming late-type galaxies and mainly passive early-type galaxies (ETGs). This evolutionary link has been extensively investigated with emphasis on the transformation of spirals into S0s via quenching their star formation (see Barr et al. 2007; Aragón-Salamanca 2008; Barway et al. 2009).

Classically, S0s comprise a spheroid-shaped bulge component and a smooth disc with little or no interstellar dust or star formation. These bulge and disc structures are well described by Sérsic ($r^{\frac{1}{n}}$; Sérsic 1963) and exponential profiles, respectively. Conversely, giant elliptical galaxies are traditionally viewed as smooth, single spheroid systems well-described by a de Vaucouleur's profile (Sérsic $n = 4$; de Vaucouleurs 1948). The morphological distinction between these two classes can be unreliable depending on disc strength, galaxy inclination, or observation depth (Kent 1985; Rix & White 1990; Jørgensen & Franx 1994; van den Bergh 2009a).

van den Bergh (1976) introduced the idea that the S0 morphology encompasses multiple distinct classes of galaxy (S0a–c; analogous to the spiral Sa–c types), differing in luminosity and evolutionary pathway (see also van den Bergh 1990, 2009b). This concept was supported by kinematic studies of S0s (e.g. Dressler & Gunn 1983), which demonstrated equivalence of the rotational properties of discs in S0s and spiral galaxies. More recently, this idea has been developed further by the ATLAS^{3D} group (e.g. Cappellari et al. 2011;

★E-mail: j.t.c.head@durham.ac.uk (JTCGH); john.lucey@durham.ac.uk (JRL)

Emsellem et al. 2011, see also Kormendy & Bender 2012). In this paradigm, most ETGs form a continuous sequence of rotating, quiescent galaxies with specific angular momentum increasing with Hubble T stage. Hence, with sufficient signal-to-noise (S/N), discs should be detectable in many galaxies classically typed as elliptical.

With increasing local environment density, the morphological fraction of galaxies becomes increasingly dominated by ETGs (particularly S0s). Conversely, spiral galaxies are rare in the dense cluster environment. This morphology–density relation (Dressler 1980) implies that the cluster environment plays an important role in the evolution of S0s from spirals (or spiral-like progenitors). The mechanisms potentially responsible for this evolution (see review in Boselli & Gavazzi 2006) can be broadly categorized as disc-fading (e.g. gas-stripping) or bulge-enhancing (e.g. tidal interactions/mergers). While the latter category is traditionally thought of as disc-disruptive, it has been demonstrated that S0 morphologies can survive merger-based quenching (Eliche-Moral et al. 2013; Querejeta et al. 2015).

The well-studied Coma Cluster (Abell 1656) possesses one of the richest ETG populations in the local Universe. As such, Coma is an excellent laboratory for studying the morphologies (e.g. Wolf 1902; Shapley 1934; Dressler 1980; van Dokkum et al. 2015) and characteristics of ETGs (e.g. Lucey et al. 1991; Bower, Lucey & Ellis 1992; Jørgensen 1999; Hudson et al. 2010; Lansbury, Lucey & Smith 2014; Weinzirl et al. 2014). In addition, Coma encompasses a wide range of environment conditions ($\sim$100 × difference in galaxy density between the core and the virial radius), allowing in-depth investigation of radial trends of environment-mediated processes (Gavazzi 1989; Guzman et al. 1992; Carter et al. 2008; Gavazzi et al. 2010; Smith et al. 2012; Cappellari 2013; Rawle et al. 2013).

In Head et al. (2014; hereafter 'Paper I'), we presented bulge–disc decompositions of $\sim$ 600 Coma Cluster galaxies, demonstrating that $\sim \frac{1}{3}$ of Coma ETGs are well described by an *archetypal* S0 (central Sérsic bulge + outer exponential disc) model morphology. Focusing exclusively on these archetypal galaxies, we found that bulges of S0 galaxies resemble pseudo-bulges ($n \sim 2$, $R_{\rm e} \sim 1$ kpc), while their discs were measured to be intrinsically smaller, or brighter than equivalent structures in star-forming spirals. A bulge–disc colour separation of $\sim$0.1 mag was measured in $g - i$ ($\sim$0.2 mag in $u - g$), indicating either an $\sim$2–3 × age difference, or an $\sim$2 × metallicity difference between these components. Nevertheless, both components were found to contribute to the galaxy red sequence (colour–magnitude) trend.

Evolutionary pathways will not necessarily preserve the archetypal S0 morphology. Furthermore, the simple exponential model (Type I; Freeman 1970) adopted in most decomposition studies does not fully represent the observed range of S0 outer disc structures. 'Broken' discs have been observed for S0 and spiral galaxies (Freeman 1970; Erwin, Pohlen & Beckman 2008), wherein surface brightness profiles beyond a break radius deviate either downwards (i.e. fainter; 'Type II') or upwards (i.e. brighter; 'Type III') relative to a simple exponential ('Type I') profile. Such profiles result from the redistribution of stars due to evolutionary processes. For example, truncated discs may be formed when stars are physically removed from a galaxy's outer regions (e.g. during tidal interaction), while antitruncated discs may result from merger events (Younger et al. 2007; Borlaff et al. 2014). Thus, investigation of galaxies with a wider range of structural morphologies provides a more complete picture of the ETG formation mechanisms.

Previous investigations of multicomponent ETG structures (e.g. Michard 1985; Capaccioli et al. 1991; Laurikainen, Salo & Buta 2005; Janz et al. 2012, 2014; Huang et al. 2013, hereafter H13; Weinzirl et al. 2014) and disc breaks (e.g. Erwin et al. 2008; Erwin, Gutiérrez & Beckman 2012; Roediger et al. 2012; Laine et al. 2014) are typically limited by (relatively) small galaxy samples from narrow fields of view or 1D profile analyses. As noted in Dullo & Graham (2014), care must be taken to report 'real' structural components, rather than overfitting galaxies with unnecessarily complex models.

Here, we build upon these pioneering studies by characterizing the multicomponent internal structures of galaxies within a wide radial area ($0 < r_{\rm cluster} < 1.3\ r_{200}$) of the Coma Cluster (and an absolute magnitude range $-17 > M_{\rm g} > -22$) using deep Canada–France–Hawaii Telescope (CFHT) i-band imaging data.

The decomposition analysis reported in Paper I is extended by using a wider suite of candidate models (including 2- and 3-component broken disc galaxies) in order to explore the diversity of galaxy structure in the Coma Cluster. Thus, we reinvestigate the structural morphologies of all Coma Cluster galaxies investigated in Paper I, including the $\sim\frac{2}{3}$ previously removed from analysis as not well-described by an archetypal bulge + disc model. While a primary goal of this analysis is the investigation of Type I, II, and III discs galaxy structures, the extended range of (multicomponent) models is necessary to avoid misclassification of additional component structures (e.g. bars or rings) as surface brightness profile breaks. Bayesian model selection and sample filtering are applied to avoid overfitting, and to ensure that best-fitting models are reliable representations of the underlying galaxy structures.

We investigate four main questions regarding galaxy evolution: Does the multicomponent structure of giant ellipticals suggest the 'puffing-up' of a compact progenitor, or the accumulation of additional structures around a compact spheroid? Are broken disc structures (truncated or antitruncated) correlated with the properties of the bulge/bar components? Do the structures of Freeman Type II galaxies indicate physical truncation of discs? Does such a truncation scenario explain the apparent size offset of S0 discs relative to star-forming spirals reported in Paper I?

The structure of this paper is as follows: first, in Section 2 we summarize the MegaCam imaging data and galaxy sample selection criteria used in this work. Secondly, Section 3 describes the multicomponent decomposition methodology, highlighting differences from the bulge–disc decomposition pipeline previously described in Paper I. Thirdly, in Section 4 we present the resulting galaxy morphology (model) fractions, including a census of disc types. Furthermore, we explore the properties of galaxies comprising multiple distinct Sérsic structures, and galaxies containing disc breaks. Finally, a discussion of possible formation pathways for broken discs is presented in Section 5.

Throughout this paper, we make use of the following notation conventions: fitted model structures (see Section 3) are indicated in italics (e.g. '*S*' for pure Sérsic) to distinguish them from morphological classifications (e.g. 'S0'). Disc break types (i.e. Freeman types; untruncated, truncated, antitruncated) are denoted with Roman numerals (e.g. 'Type II'), and galaxies containing such structures are referred to as Type I, Type II, or Type III galaxies. Conversely, galaxy types using Arabic numerals (e.g. 'Type 2') refer to Allen et al. (2006) surface brightness profile types (see also Section 3). The Type 1 profile is a special case describing a central bulge and an outer (exponential or broken exponential) disc, and is referred to as an 'archetypal S0' profile ('archetypal', or 'S0' as shorthand). All other Allen et al. (2006) types are referred to as 'atypical S0' profiles (or simply 'atypical').

We use the *WMAP*7 cosmology: $H_0 = 70.4$ km s^{-1} Mpc^{-1} (i.e. $h_{70} = 1.01$), $\Omega_{\rm m} = 0.272$, and $\Omega_\Lambda = 0.728$ (Komatsu et al. 2011).

Using $z_{\rm CMB}$(Coma) = 0.024, the luminosity distance for the Coma Cluster is 104.1 Mpc, and the distance modulus, $m - M = 35.09$. At this distance, 1 arcmin corresponds to 28.9 kpc. Taking a value for velocity dispersion of $\sigma_{\rm Coma} = 1008$ km s^{-1} (Struble & Rood 1999) and virial mass, $M_{200} = 5.1 \times 10^{14}\, h_{70}^{-1}$ M$_{\odot}$ (Gavazzi et al. 2009), the virial radius, r_{200}, for Coma is 2.2 Mpc (∼75 arcmin).

2 DATA AND INITIAL SAMPLE

This study makes use of the data as previously described in Paper I. To recap: optical imaging covering a total of 9 deg^2 of the Coma Cluster in the *i* band was acquired using the MegaCam instrument on the 3.6 m CFHT during 2008 March–June (run ID 2008AC24, PI: M. Hudson). Total (co-added) exposure times of 300 s were obtained for each observed field, yielding ∼12 × deeper imaging data (from $D^2 t_{\rm exp}$) compared to SDSS (2.5 m telescope, 53 s exposures). The MegaCam frames were sky-subtracted during pre-processing using a 64 pixel mesh. A point spread function (psf) full width at half-maximum of between 0.65 and 0.84 arcsec was typical. The pixel scale was ∼0.186 arcsec pixel^{-1}.

The initial sample for analysis was selected from SDSS (DR9) catalogue galaxies in the 3 deg × 3 deg (≡5.2 Mpc × 5.2 Mpc, $2r_{200} \times 2r_{200}$) area covered by the MegaCam observations. A limit of $-17.1 > M_{\rm g}$[1] was applied to ensure sufficient S/N for reliable measurement of galaxy bulge and disc structures. These targets were limited to the redshift range $0.015 < z < 0.032$ (heliocentric $v_{\rm Coma} \pm 2.5\sigma_{\rm 1D}$) to ensure that only cluster members were included. Unlike Paper I, no colour cut is made during sample selection. Thus, an additional ∼60 blue galaxies ($g - r \leq 0.5$) are included in this work, yielding an initial sample of 631 Coma Cluster members.

To illustrate the initial image analysis undertaken, and the diversity of photometric structures observed, we show in Fig. 1 the major axis surface brightness profiles for six representative Coma galaxies. As well as displaying the profile derived from the stacked image data *(black points)*, we show the results from the individual MegaCam exposures *(grey lines)*. The radial limit used in our profile analysis is shown *(grey vertical bars)*; this corresponds to 1–3 per cent of the sky brightness level (*i* band ≃25 mag arcsec^{-2}). Within the fitted area, there is very good agreement between the stack and individual image profiles. This demonstrates that the stacking process, including the choice of sky-grid mesh size, has little or no effect on the derived profiles and hence on the 2D surface fitting analysis reported below.

Here we briefly note some of the key features apparent in the surface brightness profiles for these six galaxies. Galaxy 1237667322723369088 has a distinct break in profile at ∼8 arcsec with a second, downward-bending exponential-like outer shape. 1237667444048593359 has a slight upward-bending outer structure, although this may be affected by the nearby contaminating galaxy. 1237667323797504020 displays a relatively weak intermediate exponential-like structure, and an outer downward-bending shape. 1237667444048527399 has a very distinctive upward-bending, exponential-like outer structure. 1237667444585595093 has a weak, downward-bending exponential-like outer structure. 1237667442974392369 has a weak, upward-bending outer structure.

In Section 4 the model surface brightness profiles for these six galaxies derived from the multicomponent fits are shown overplotted on the data points. Work in progress will provide a detailed comparison of the surface brightness profiles of Coma Cluster galaxies derived from a wide variety of independent imaging sources (MegaCam, *HST* ACS, SDSS, Pan-STARRS, etc.).

[1] Note that while the sample is defined based on *g*-band photometry, we analyse the *i*-band data in this paper.

3 ANALYSIS

3.1 Decomposition

Galaxy decomposition was carried out using GALFIT (version 3.0.4; Peng et al. 2010) with an automated PYTHON wrap-around derived from AGONII (Automated Galfitting of Optical and Near Infra-red Imaging; Paper I). Details of this fitting procedure (including description of the extraction and calibration of input MegaCam data products) can be found in Appendix B2 and Paper I.

In this work, we fit galaxies with a range of analytical models in order to thoroughly explore the diversity of internal galaxy structures. These candidate models are comprised of one to three structural components, each described by one of four functional forms (see Table 1): exponential 'discs' ('*D*'), general Sérsics ('*S*'), boxy Sérsics ('*C*'), and broken discs ('*Dd*'). Note that the central *S* component in any model is referred to as the bulge, and labelled as '*B*'. Conversely, non-central *S* components in models containing a disc are referred to here as 'bars'. However, this convention does not explicitly require a stellar bar structure. As such, a 'bar' may also correspond to a lens or oval structure. The broken disc component (see Appendix B4) comprises inner and outer exponential discs (with differing scalelengths, $R_{\rm s,in}$ and $R_{\rm s,out}$) connected by a smooth transition at a break radius ($r_{\rm brk}$).

The 10 candidate multicomponent models considered in this work are catalogued in Table 2. Sérsic-only (hereafter '*S*') and bulge + disc (hereafter '*BD*') models are unchanged from those presented in Paper I. In addition, we present the decomposition results when boxy bulge + disc (hereafter '*CD*'), double Sérsic (hereafter '*BS*'), bulge + double disc (hereafter '*BDD*'), bulge + bar + disc (hereafter '*BSD*'), bulge + double Sérsic (hereafter '*BSS*') models are also considered. Three further models variants implement the 'broken disc' profile: bulge + broken disc (hereafter '*BDd*'), boxy bulge + broken disc (hereafter '*CDd*') and bulge + bar + broken disc (hereafter '*BSDd*'). In order to avoid fitting bias due to the choice of initial parameter values, model inputs are based on the best-fitting parameters of simpler model types (e.g. *BSD* input derived from best *BD* fit). This iterative build-up of model complexity significantly improves reliability of the measured galaxy properties, particularly for highly degenerate multicomponent models.

We use Allen et al. (2006) types to describe the relationship between the bulge (i.e. innermost Sérsic) and (exponential or broken) disc profiles (see Appendix B3). This convention is also used for 3-component model systems, as fewer constraints are place on bar/disc or bulge/bar morphology. The only exception in which attention is paid to these profile interactions is where profile inversion implies incorrect interpretation of the model components (i.e. 'Type 4' bulge/bar or bar/disc structures; see also Appendix B5).

3.2 Model selection and results filtering

Sample filtering is applied to the fitting results (similar to Paper I) in order to isolate a sample of accurately fit galaxies. A key step in this process is the selection of best-fitting models which are meaningful descriptions of each galaxy's underlying morphological structure, ensuring that all structural components are statistically justified. Galaxy models are assessed on both

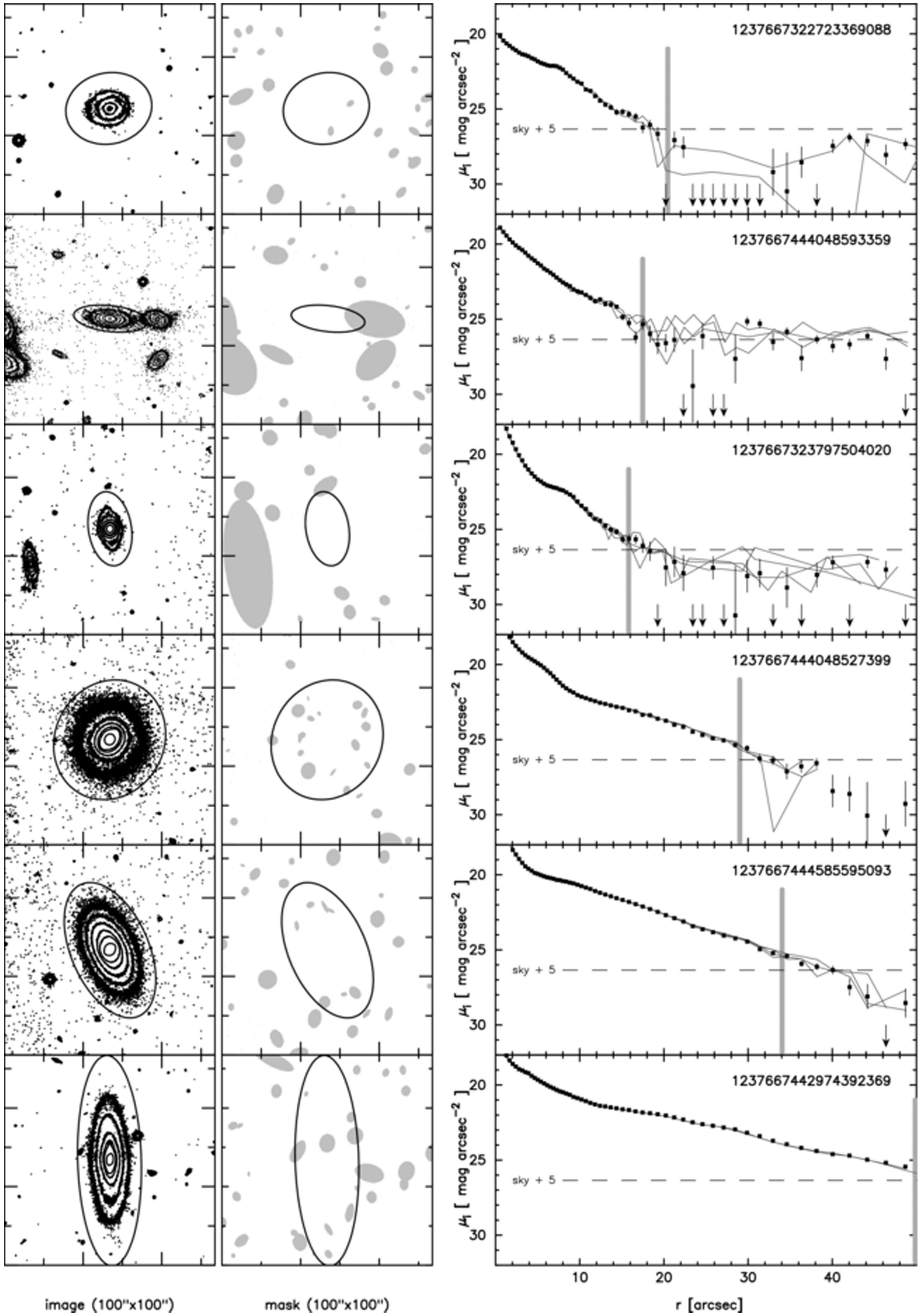

Figure 1. Diversity of surface brightness profiles observed in the Coma Cluster galaxies. Six representative galaxies are shown. The first panel of each row is the galaxy thumbnail image contour plot (100 arcsec × 100 arcsec). The second panel shows the areas masked in the fitting procedure. The ellipses in these two panels denote the extent of the galaxy area fitted. The third panel shows the major axis surface brightness profiles (30° width wedges) and errors as derived from the stack MegaCam images; labelled by the SDSS `ObjID` number. The measured profiles derived from the individual MegaCam exposures are shown as grey lines. The 1 per cent level of the sky brightness is shown as the horizontal dashed line. The vertical grey bar shows the radius limit used in the fitting.

Table 1. Table of the model components used during decomposition analysis, including descriptions of their free parameters. Note that the 'bulge' label (B) is used to describe the central Sérsic component. All components in a model share centroid position parameters (x, y). C_0 is defined in Peng et al. (2010).

Component	Parameter	Description
D	m_i	Total i-band magnitude
	R_s	Exponential scalelength
	q	Axis ratio (b/a)
	Φ	Position angle
B or S	m	Total i-band magnitude
	R_e	Effective half-light radius
	n	Sérsic index
	q	Axis ratio (b/a)
	Φ	Position angle
C	m	Total i-band magnitude
	R_e	Effective half-light radius
	n	Sérsic index
	q	Axis ratio (b/a)
	Φ	Position angle
	C_0	Boxiness/Disciness parameter
Dd	$\mu_{\rm brk}$	Surface brightness at $r_{\rm brk}$
	$R_{\rm s,in}$	Inner exponential scalelength
	$R_{\rm s,out}$	Outer exponential scalelength
	$r_{\rm brk}$	Break radius
	q	Axis ratio (b/a)
	Φ	Position angle

Table 2. Table of the multicomponent models used during decomposition analysis, including the number of independent structural components, $n_{\rm comp}$, and number of free parameters, k.

Model	Label	k	$n_{\rm comp}$
Sérsic	S	7	1
Sérsic + exponential	BD	11	2
Boxy Sérsic + exponential	CD	12	2
Double Sérsic	BS	12	2
Sérsic + broken exponential	BDd	13	2
Boxy Sérsic + broken exponential	CDd	14	2
Sérsic + double exponential	BDD	15	3
Double Sérsic + exponential	BSD	16	3
Triple Sérsic	BSS	17	3
Double Sérsic + broken exponential	$BSDd$	18	3

goodness-of-fit (i.e. ensuring that a galaxy is neither underfitted nor overfitted), and suitability of component structures (i.e. rejecting components with unrealistic parameters, or which do not measure the intended target substructure). By removing such instances of dissonance between the galaxy and model structures, the reliability of multicomponent analysis results is vastly improved. A detailed description of the galaxy filtering conditions, and a flow chart illustrating the overall filtering process is presented in Appendix B5.

Galaxies are initially assessed for asymmetry (via the A parameter; Homeier et al. 2006) and contamination (via image mask fraction, $f_{\rm mask}$) to ensure robust measurements of galaxy properties. Highly asymmetric galaxies, or galaxies strongly contaminated by neighbouring sources cannot be reliably fit by smooth, symmetric models, and are thus removed from consideration. Due to high parameter uncertainty, galaxies are also removed if their best-fitting models are poorly fitted (high χ^2_ν), highly inclined to the line of sight (from the axis ratio of the outer component), or if a model component contributes less than 5 per cent of the total galaxy luminosity (component fraction, C/T<0.05). Additional filtering conditions are placed on broken disc galaxies to ensure that both the inner and outer disc contribute significantly to the overall galaxy profile, and to avoid erroneous regions of parameter space.

Selection between alternative candidate models is made using the Bayesian Information Criterion (BIC; Schwarz 1978), calculated over independent resolution elements (see details in Paper I). This is defined as

$$\mathrm{BIC}_{\rm res} = \frac{\chi^2}{A_{\rm psf}} + k\,\ln\left(\frac{n_{\rm pix}}{A_{\rm psf}}\right), \quad (1)$$

where χ^2 is the standard (unreduced) fitting chi-squared, k is the number of model parameters (degrees of freedom), $n_{\rm pix}$ is the number of image pixels used during fitting, and $A_{\rm psf}$ is the area of a resolution element (in pixels). Here, $A_{\rm psf}$ is calculated as the area within two standard deviations (σ) of the psf image centre, as measured by fitting a Gaussian model. For a set of candidate models, the model with the lowest $\mathrm{BIC}_{\rm res}$ maximizes goodness-of-fit without introducing unnecessary free parameters (hereafter 'best-fitting' model). This ensures that each of the best-fitting model components provide a statistically significant improvement to χ^2.

Measurement error in $A_{\rm psf}$ leads to an associated uncertainty in $\mathrm{BIC}_{\rm res}$ ($\sigma_{\rm res}$). Therefore, a $3\sigma_{\rm res}$ reduction in $\mathrm{BIC}_{\rm res}$ is required before a more complex (higher k) model is accepted as a statistical improvement over a simpler model. This 3σ selection condition is based on comparison with by-eye classification, and is discussed in further detail in Paper I, and Head (2014). Here, $\sigma_{\rm res}$ is based on the scatter in $A_{\rm psf}$ (typically ~3 per cent), as measured across multiple star images. For example, a galaxy fit by S and BD models yields $\mathrm{BIC}_{\rm res}$ values of 3500 and 3450 (respectively) with an associated $\sigma_{\rm res}$ of 10. Since $\Delta\mathrm{BIC}_{\rm res} = 50 > 3\sigma_{\rm res}$, the addition of the exponential disc component is a statistically significant improvement to the fit, and hence measures a distinct photometric structure.

4 RESULTS

4.1 Best-fitting models

A wide mix of best-fitting model morphologies are found for the 631 galaxies (570 Coma sample + 61 blue Coma galaxies) investigated (see example plots in Appendix A). The fractions of galaxies best described by each candidate multicomponent model are illustrated in Fig. 2. From the initial sample (N = 631), 162 are best fitted by a Sérsic-only model (26 per cent), 102 are best fitted by BD (16 per cent), 43 are best fitted by BS (7 per cent), 3 are best fitted by CD (<1 per cent), 18 are best fitted by BDd (3 per cent), 3 are best fitted by CDd (<1 per cent), 43 are best fitted by BDD (7 per cent), 97 are best fitted by BSD (15 per cent), 98 are best fitted by BSS (16 per cent), and 62 are best fitted by $BSDd$ (10 per cent). Thus, the majority of Coma Cluster galaxies (58 per cent) have morphologies more complex than the simple S and BD models.

Many of these complex structure galaxies were considered to be (archetypal S0) bulge + disc systems in Paper I. In total, 51 'archetypal' galaxies (from N = 200; 25.5 per cent) remain best fit by a BD model, while 129 (64.5 per cent) require more complex models and 20 (10.0 per cent) are demoted to a single-Sérsic model (due to the more stringent model selection tests in this work). The fractions of prior 'atypical bulge + discs' adequately fit by a

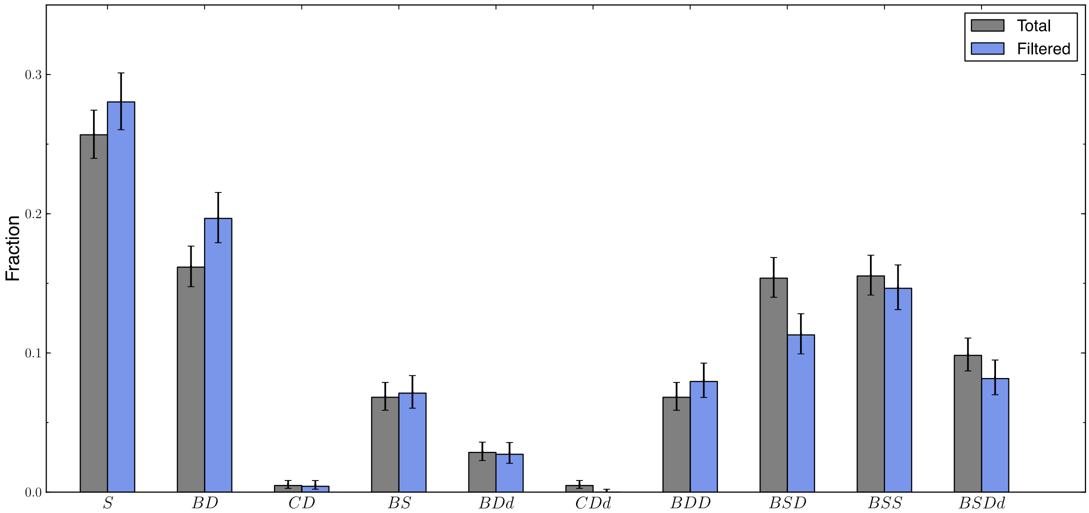

Figure 2. Histogram of best-fitting model type fractions for the initial ($N = 631$) and filtered ($N = 478$) samples. Error bars are 68 per cent confidence limits.

BD model (21.1 per cent of 137), requiring more complex models (73.0 per cent), and demoted to *S* (5.8 per cent) are similar. Note that many galaxies classed as 'unstable' previously are best fit here by complex 3-component models (68 per cent of 128). This is due to significant reductions in χ^2_ν as additional structural components are accounted for.

After sample filtering (see Section 3.2), 478 galaxies from the sample of 631 (76 per cent) remain. The 153 galaxies removed by filtering comprise 80 galaxies removed due to asymmetry or contamination, 23 galaxies with high χ^2, 13 highly inclined galaxies, 3 galaxies with anomalous outer discs due to $R_{\mathrm{s,out}} > 0.1\ r_{\mathrm{brk}}$, 2 galaxies with anomalous inner discs due to $r_{\mathrm{brk}} < 5$ arcsec, and 32 galaxies removed due to inverted Sérsic/disc components (i.e. disc-dominated at low radii, Sérsic-dominated at large radii). From the remaining filtered sample, 134 galaxies are best fitted by a Sérsic-only model (28.0 per cent), 94 are best fitted by *BD* (20 per cent), 34 are best fitted by *BS* (7 per cent), 2 are best fitted by *CD* (<1 per cent), 13 are best fitted by *BDd* (3 per cent), none are best fitted by *CDd*, 38 are best fitted by *BDD* (8 per cent), 54 are best fitted by *BSD* (11 per cent), 70 are best fitted by *BSS* (15 per cent), and 39 are best fitted by *BSDd* (8 per cent).

Note that in total, 93 galaxies (20 ± 2 per cent) are well described by 'barred' models (*BSD*, *BSDd*). This barred fraction for Coma is significantly lower than the value reported in Lansbury et al. (2014) from either decomposition (72^{+5}_{-6} per cent) or ellipse (48 ± 6 per cent) analyses. This difference cannot be reconciled, even if *BSS* models are included in the 'barred' sample (yielding 34^{+3}_{-2} per cent bar fraction). However, if the present sample is restricted to only contain galaxies with D80 morphological classifications (as in Lansbury et al. 2014), then the barred fraction (including *BSS* galaxies) rises to 63 ± 4 per cent. This fraction rises further if only D80 S0s (including S0/a, E/S0) galaxies are considered, yielding bars in 71 ± 5 per cent of galaxies. As the D80 catalogue only covers the bright end of the Coma sample ($M_g \lesssim -18$), the bar fraction increase for D80 galaxies indicates a significantly decreasing bar detection rate for faint galaxies. However, the lower bar detection rate relative to Lansbury et al. (2014), particularly if *BSS* galaxies are not considered 'barred', reflects the more stringent conditions for accepting a more complex model in this work.

Structural biases in decomposition studies with overly simplistic galaxy models can be quantified by artificially limiting the range of candidate models considered during model selection. If model selection were repeated *without* considering double/triple Sérsic models, 94 out of 631 galaxies (20 per cent) would be identified as best fitted by models including a broken disc (*BDd*, *CDd*, *BSDd*). Of these, 42 galaxies are better described by a double or triple Sérsic model. Thus, a 2D decomposition analysis falsely reports broken disc models 45 per cent of the time if only models with exponential discs are considered. Alternatively, if 3-component models are excluded from consideration for 2D analysis, a 2-component model is preferred in 342 galaxies (72 per cent of total). However, 199 of these galaxies would be better fit by a 3-component model.[2] Thus, 2D analysis selects an overly simplistic 2-component model 58 per cent of the time if 3-component models are not considered.

Of all 141 galaxies with 2-component structures, 82 galaxies (58 per cent) exhibit Type 1 (i.e. 'archetypal' inner + outer component) profiles, while 44 Type 3 profile galaxies (recurrent bulge; 31 per cent) make up the second most common structural type. For 3-component systems ($N = 201$), a larger proportion of galaxies (130; 65 per cent) are characterized by Type 1 bulge/disc structures, while only 55 galaxies (27 per cent) had Type 3 bulge/discs. Thus, 2- and 3-component galaxies have archetypal bulge + disc structures in the majority of cases, with recurrent bulges (dominant over their discs at large radii) being the second most common structure.

If a *BD* model is forced on the 478 galaxies in the filtered sample, 214 (62 per cent) yield a Type 1 (archetypal) profile, and 72 galaxies (21 per cent) correspond to a Type 3 (recurrent bulge) profile. These profile fractions do not change significantly if galaxies best fitted by a 2- or 3-component model are considered separately (Type 1/3: 66 per cent/20 per cent for 2-component galaxies, 59 per cent/22 per cent for 3-component galaxies). Thus, Type 3 *BD* profiles do not intrinsically represent underfit galaxy structures, but rather a structural morphology distinct from archetypal bulge + disc systems.

In summary, thorough 2D decomposition analysis reveals a rich range of galaxy structures in the Coma Cluster, with 3(+) structural components required in 42 per cent of galaxies. 2+

[2] Disparity between this value and the 201 3-component models reported above is due to two galaxies which would be better fit by a single Sérsic model, if 3-component models are excluded.

Table 3. Table of the median structural parameter values for multi-Sérsic model galaxies (*S*, *BS*, *BSS*), indicating the half-light radii, Sérsic indices, component axis ratios (q), and component fraction (C/T) of each model component. In addition, the median total apparent magnitude (m_i), and number of galaxies (N) are given for each model type.

Model	Parameter	Comp. 1	Comp. 2	Comp. 3
S	n	1.90 ± 0.05	–	–
	R_e [kpc]	1.99 ± 0.07	–	–
$N = 134$	q	0.63 ± 0.02	–	–
$m_i = 16.58 \pm 0.03$	C/T	1.0	–	–
BS	n	2.12 ± 0.30	0.66 ± 0.10	–
	R_e [kpc]	5.27 ± 0.90	14.57 ± 0.90	–
$N = 34$	q	0.66 ± 0.04	0.79 ± 0.04	–
$m_i = 15.76 \pm 0.12$	C/T	0.35 ± 0.04	0.65 ± 0.04	–
BSS	n	2.17 ± 0.23	0.43 ± 0.13	0.55 ± 0.04
	R_e [kpc]	4.20 ± 0.55	12.68 ± 0.76	25.80 ± 1.75
$N = 70$	q	0.71 ± 0.03	0.48 ± 0.04	0.58 ± 0.04
$m_i = 14.45 \pm 0.08$	C/T	0.42 ± 0.02	0.26 ± 0.02	0.27 ± 0.02

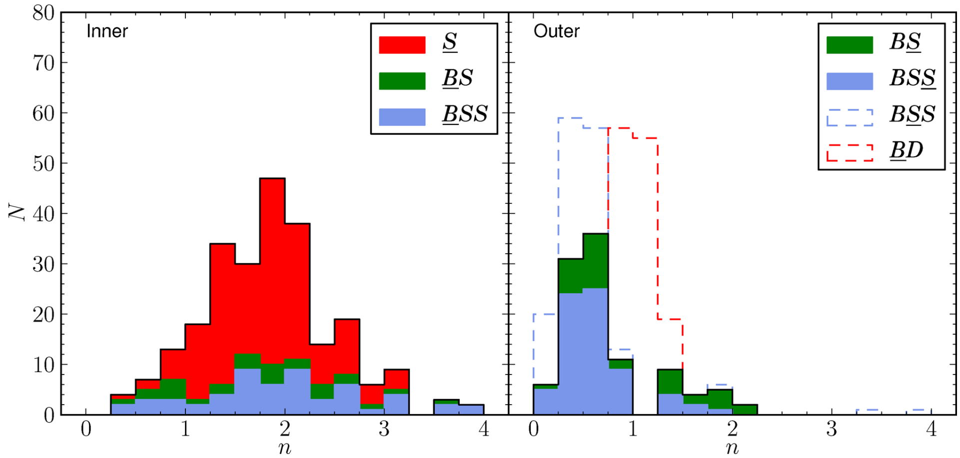

Figure 3. Histograms of Sérsic index, n, for multicomponent Sérsic galaxies. Left: the n distribution for inner-dominant Sérsic structures (***S***, ***B**S*, ***B**SS*), divided by best-fitting model type. Right: the n distribution of outer-dominant Sérsic structures (*B**S***, *BS**S***) divided by best-fitting model type. The equivalent distributions including middle Sérsic structures (*B**S**S*) or outer Sérsic n for *BS* fits to galaxies best fitted by a *B**D*** model are included as dashed blue and red histograms, respectively.

component structure systems were well represented by archetypal (central) bulge + (outer) disc morphologies in the majority of cases ($N = 202$), including 52 galaxies which exhibited broken disc profiles. This broken disc fraction would be overestimated, however, if multicomponent models (including double/triple Sérsic systems) were not considered during model selection.

4.2 Multi-Sérsic structures

From the initial sample of 478 galaxies (filtered to exclude badly fit galaxies; see Section 3.2), ∼50 per cent were best described by a model comprising one or more Sérsic components (28 per cent *S*; 7 per cent *BS*; 15 per cent *BSS*).[3] In this section, we briefly discuss the structural results for these multicomponent Sérsic galaxies (Table 3). Note that average galaxy luminosity increases with number of model components, highlighting the strong S/N and spatial size dependence of multicomponent structure detection.

Fig. 3 illustrates the distributions of n for inner (left-hand panel) and outer (right-hand panel) Sérsic components. In all Sérsic model variants, the central structure is compact and has a 'pseudo-bulge-like' ($n \sim 2$) profile. For *S* model galaxies, the Sérsic structure is equivalent to a 'naked' bulge for *BD* galaxies, albeit a factor of 2 times larger ($R_\mathrm{e} \sim 2$ kpc). The central 'bulges' of both *BS* and *BSS* galaxies are consistent in size, but larger on average than a single Sérsic ($R_\mathrm{e} \sim 4$ kpc). Note that very few inner structures refer to a classic $n = 4$ (de Vaucouleur's) profile. If *BSS* (or other 3-component) galaxies were force fit by a single Sérsic structure, however, the resulting n distribution would extend to $n \sim 8$, peaking strongly for $n = 3$–4. Hence, de Vaucouleur's profile may arise from underfitting more structurally complex systems.

Outer Sérsic structures have Gaussian-like profiles ($n \sim 0.5$) on average, although a weak tail exists in the n distribution towards higher values (Fig. 3, right-hand panel). Since an outer component with $n = 1$ would be described by a *BD* model, the $1.00 < n < 1.25$ bin is empty for outer structures. If the disc n is allowed to vary for

[3] Note that outer Sérsic $n \neq 1$ for these models. Thus, we exclude the *BD* and *BSD* models as special cases of *BS* and *BSS*.

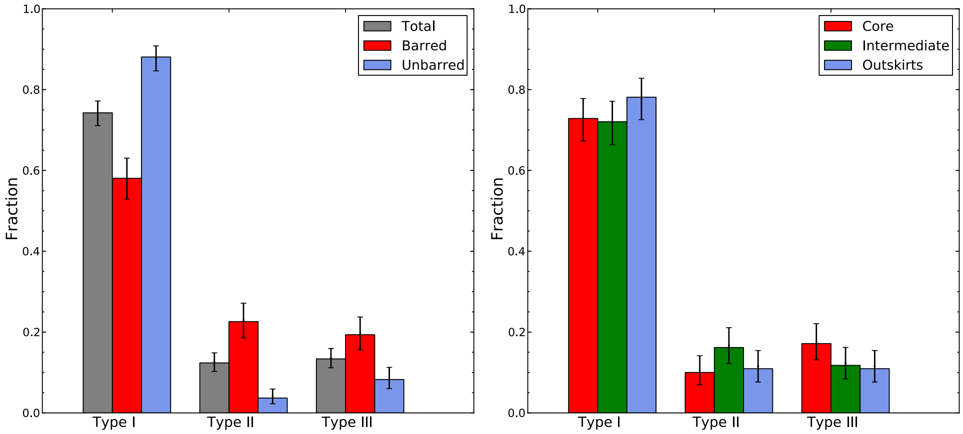

Figure 4. Histogram of outer disc type fractions for (left) barred (*BSD*, *BSDd*) and unbarred (*BD*, *BDd*) bulge + disc models, (right) galaxies in the core ($r_{\rm cluster} < 800$ kpc), intermediate ($0.8 < r_{\rm cluster} < 1.6$ Mpc), and outskirts ($r_{\rm cluster} > 1.6$ Mpc) cluster samples. Types I, II, and III refer to unbroken, truncated, and antitruncated discs, respectively. Error bars are 68 per cent confidence limits.

these bulge + disc galaxies (i.e. fitting a *BS* model), then a continuous distribution of outer structure Sérsic index becomes apparent (red dashed histogram in Fig. 3). The resulting 'disc' n distribution covers the range $0.5 < n < 1.5$, but peaks strongly at $n = 1$ (median value: 1.00, standard deviation: 0.24).[4] Hence, a subset of the outer structures considered in this section may represent ($n \neq 1$) discs. This is supported by the detection of rapid galaxy rotation ($V_c > 100$ km s^{-1}) for 11 of our 70 *BSS* galaxies in Rawle et al. (2013; $\sim\frac{1}{3}$ of their S0 sample). However as a practical choice, only $n = 1$ discs will be considered in discussion of disc structure in later sections due to the uncertain nature of outer Sérsic structures.

The outer and middle Sérsic structures of *BS* and *BSS* galaxies are both $\gtrsim$10 kpc larger than 'bulges', but represent drastically different fractions of their parent galaxy's total luminosity ($\sim\frac{2}{3}$ and $\sim\frac{1}{4}$, respectively). Conversely, the outer structure of *BSS* galaxies is comparable in luminosity to the middle Sérsic , but is an additional 10 kpc larger. As such, *BSS* galaxies are structurally equivalent to *BS* galaxies with the addition of an outer Sérsic structure. The outer Sérsic structures may be the remnants of past merger events. As such, the distinction between *BS* and *BSS* may be a difference in the number of major merger events experienced in the past.

By comparison, the triple Sérsic structures measured by Huang et al. (2013; H13) in a small sample of nearby (visually selected) ellipticals consist of a faint, compact central object ($R_{\rm e} < 1$ kpc), a middle component ($R_{\rm e} \sim 2.5$ kpc), and a dominant outer envelope ($R_{\rm e} \sim 10$ kpc). If the compact components are neglected, the H13 structures are comparable with the multi-Sérsic models in this work, albeit with smaller bulges, and more centrally concentrated outer profiles ($n \sim 1$–2 in H13). This discrepancy in outer component n may indicate that the outer profiles in H13 encompass multiple distinct Gaussian structures (e.g. both outer Sérsic components in our *BSS* galaxies). Alternatively, given the low local environment density of galaxies in the H13 sample, the increased detection rate of weak additional outer Sérsic structures in this work may instead reflect a more active merger history of present-day Coma Cluster galaxies. This is supported by the higher average bulge size in this work, as mergers will also increase bulge $R_{\rm e}$.

If the *BS* and *BSS* models considered in this section represent the multicomponent structures of traditional elliptical galaxies, then such galaxies comprise a (relatively) compact pseudo-bulge (∼5 kpc) around which large (∼10–20 kpc) outer (Gaussian) structures have been assembled. These compact central structures are 2–3 × larger than 'red nugget' objects (∼1–2 kpc) detected at high redshift ($z \sim 2$; Damjanov et al. 2009). Thus, if the multicomponent Sérsic galaxies observed in Coma in this work evolved from red nuggets, then their bulge structures must have experienced significant size growth ('puffing up'). However, the *total* effective radii for *BS* and *BSS* galaxies (estimated from the combined luminosities of all model components, assuming alignment of component position angles – PAs) is ∼10–11 kpc on average,[5] suggesting an even more drastic growth mechanism (∼6 times, consistent with van Dokkum et al. 2014).

In summary, galaxies comprising multiple Sérsic structures (with outer $n \neq 1$) resemble a compact central pseudo-bulge (reminiscent of single Sérsic systems; $n \sim 2$, $R_{\rm e} \sim 4$ kpc) embedded in extended Gaussian ($n \sim 0.5$) envelopes. The combined effective half-light radii of these systems typically exceeds 10 kpc. Thus, if multi-Sérsic galaxies evolved from compact 'red nuggets' as detected at high redshift, then such systems must have experienced an $\gtrsim 6 \times$ increase in size.

4.3 Freeman disc type fractions

Galaxies with single disc-like outer profiles (*BD*, *CD*, *BDd*, *CDd*, *BSD*, *BSDd*) were categorized by their disc types (i.e. Freeman Type I, II, or III). In total, 202 valid disc galaxies are contained within the sample after filtering. Of these, 150 galaxies (74 ± 3 per cent) have Type I (untruncated) discs, 25 galaxies (12^{+3}_{-2} per cent) have Type II (truncated) discs, and 27 galaxies (13^{+3}_{-2} per cent) have Type III (antitruncated) discs (Fig. 4, left-hand panel). Compared to the disc type fractions reported in the Virgo cluster (Type I: 46 ± 10 per cent, Type II: 0^{+4}_{-0} per cent, Type III: 54 ± 10 per cent; Erwin et al. 2012),

[4] Recall, however, that these changes in outer profile n do not yield statistically significant improvements to the goodness-of-fit relative to fixing $n = 1$.

[5] Even if the outermost structures in *BSS* galaxies were dismissed as fitting artefacts, the total $R_{\rm e}$ of such systems would remain in excess of 7 kpc.

Table 4. Table of the average structural parameter values for Type I/II/III archetypal disc galaxies with simple exponential discs (*BD*, *CD*, *BSD*) and broken exponential discs (*BDd*, *BSDd*). The average Sérsic indices (n), half-light radii (R_e), component axis ratio (q), and component fractions (C/T) are indicated for each model component. For Type II and III galaxies, both the inner and outer R_e ($=1.678R_s$) are included. In addition, the median total apparent magnitude (m_i), and number of galaxies (N) are given for each disc type.

Disc type	Parameter	B	S	D/Dd
Type I	n	1.52 ± 0.09	0.44 ± 0.04	1.0
	R_e [kpc]	0.62 ± 0.04	1.94 ± 0.16	3.68 ± 0.18
$N = 97$	q	0.65 ± 0.02	0.54 ± 0.04	0.67 ± 0.02
$m_i = 15.82 \pm 0.10$	C/T	0.27 ± 0.02	0.11 ± 0.02	0.62 ± 0.02
Type II	n	2.32 ± 0.14	0.44 ± 0.04	1.0
	R_e [kpc]	0.96 ± 0.07	2.91 ± 0.22	9.28 ± 1.44 / 4.12 ± 0.20
$N = 18$	q	0.69 ± 0.05	0.49 ± 0.08	0.56 ± 0.05
$m_i = 14.65 \pm 0.12$	C/T	0.33 ± 0.04	0.21 ± 0.03	0.46 ± 0.04
Type III	n	1.74 ± 0.19	0.43 ± 0.03	1.0
	R_e [kpc]	0.54 ± 0.05	2.82 ± 0.49	3.58 ± 0.20 / 5.62 ± 0.34
$N = 24$	q	0.70 ± 0.04	0.39 ± 0.07	0.54 ± 0.05
$m_i = 14.49 \pm 0.17$	C/T	0.24 ± 0.04	0.14 ± 0.02	0.62 ± 0.03

we detect significantly more Type I and II discs in Coma, but fewer Type III discs. By comparison, the field S0 sample in Erwin et al. (2012) yields significantly fewer Type I discs (26^{+7}_{-6} per cent), but greater Type II (28^{+7}_{-6} per cent) and III (46 ± 7 per cent) fractions than the Coma sample.

If considered separately, Type I discs are found more frequently in unbarred (*BD*, *CD*, *BDd*, *CDd*; 88 ± 3 per cent) galaxies than those containing bars (*BSD*, *BSDd*; 58 ± 5 per cent). Consequently, barred galaxies have a greater fraction of Type II and III discs (23^{+5}_{-4} and 19 ± 4 per cent) than galaxies without bars (4^{+2}_{-1} and 8^{+3}_{-2} per cent). Erwin et al. (2012) also reported a decrease in the Type I fraction for barred Virgo galaxies (23^{+9}_{-7} per cent); however, the increased barred Type II fraction in this work only widens the disparity between Coma and Virgo Type II disc detection. Note that no strong correlation (Pearson's $\rho \sim 0.3$) is detected between bar and broken disc axis ratios (q) of *BSDd* galaxies, indicating that these model components are structurally distinct. Thus, the detection of a large number of broken discs in barred galaxies is not an artefact of overfitting (i.e. via coupling of the inner disc to the Sérsic bar profile).

To test the variation of disc type with environment, the filtered Coma sample was subdivided into core, intermediate, and outskirts samples based on galaxy distance from the cluster centre ($r_{\rm cluster} < 0.8$ Mpc, $0.8 < r_{\rm cluster} < 1.6$ Mpc, and $r_{\rm cluster} > 1.6$ Mpc, respectively; Fig. 4, right-hand panel). These cluster-centric radial ranges are selected such that each sample has approximately equal occupancy ($N = 70$, 68, and 64). In all three samples, Type I discs form the vast majority, with a slightly increased Type I disc fraction for outskirt galaxies (73^{+5}_{-6}, 72^{+5}_{-6}, and 78^{+5}_{-6} per cent for core, intermediate, and outskirt galaxies). Type II and III disc fractions are consistent across all radial samples (Type II: 10^{+4}_{-3}, 16^{+5}_{-4}, 11^{+5}_{-3} per cent; Type III: 17^{+5}_{-4}, 12^{+4}_{-3}, 11^{+5}_{-3} per cent) although slight peaks in Type II and Type III disc fractions are apparent in the intermediate and core samples (respectively).

In summary, greater fractions of Freeman Type I (untruncated; 74 per cent) and Type II (truncated; 12 per cent) discs were detected in this work than have been reported previously in the Virgo cluster. Conversely, the measured fraction of Type III (antitruncated) discs in Coma (13 per cent) was lower than Virgo. The majority of galaxies with Type II or III discs also contain galaxy bars (Type II: 89 per cent; Type III: 71 per cent), compared to less than half of galaxies with unbroken discs (Type I: 42 per cent). No significant variation in Type I/II/III fraction was detected with local environment within Coma.

4.4 Freeman Type I, II, and III galaxy structures

In this section, the galaxy sample is divided by Freeman type to investigate differences in internal structure for galaxies with untruncated (Type I), truncated (Type II), or antitruncated (Type III) discs. We consider all models with a single (exponential) disc component which dominates (relative to the bulge) at large galaxy-centric radii (*BD*, *CD*, *BDd*, *BSD*, *BSDd*). Here, the distributions and trends in structural parameters for galaxies with (single) disc-dominated outer regions (*BD*, *CD*, *BDd*, *BSD*, *BSDd*) are investigated. In order to ensure that model parameters are measured from consistent structures (i.e. exponential/broken exponential components measure galaxy disc properties), we only consider galaxies with archetypal bulge/disc models (i.e. Type 1; central bulge + outer disc). This reduces the sample of analysed galaxies to 146 (67 2-component galaxies, 79 3-component galaxies), of which 97 galaxies have Type I discs, 18 have Type II discs, and 24 have Type III discs. The average structural properties and total magnitudes of archetypal galaxies containing discs of each type are summarized in Table 4. Example surface brightness profiles for (*BDd* and *BSDd*) galaxies with Type II and Type III discs are presented in Fig. 5. As a convenient shorthand, we hereafter use the phrase 'Type I/II/III galaxy' to refer to galaxies containing Freeman Type I/II/III discs.

4.4.1 Central components of Type I/II/III galaxies

The bulge and bar Sérsic indices for galaxies of each disc type are presented in Fig. 6. Bulge n is smaller (on average) in Type I (1.89 ± 0.08) galaxies those with Type II (2.32 ± 0.14) broken discs, and consistent with the bulges of Type III galaxies (1.74 ± 0.19). By comparison, *bar* Sérsic index is consistent across all Freeman types (0.44 ± 0.04 for Type I, 0.44 ± 0.04 for Type II, and 0.43 ± 0.03 for Type III). Thus, while consistent bar profiles are measured independent of disc type, the bulge profile shape depends on disc structure. Note that the Type I averages are calculated from galaxies in the

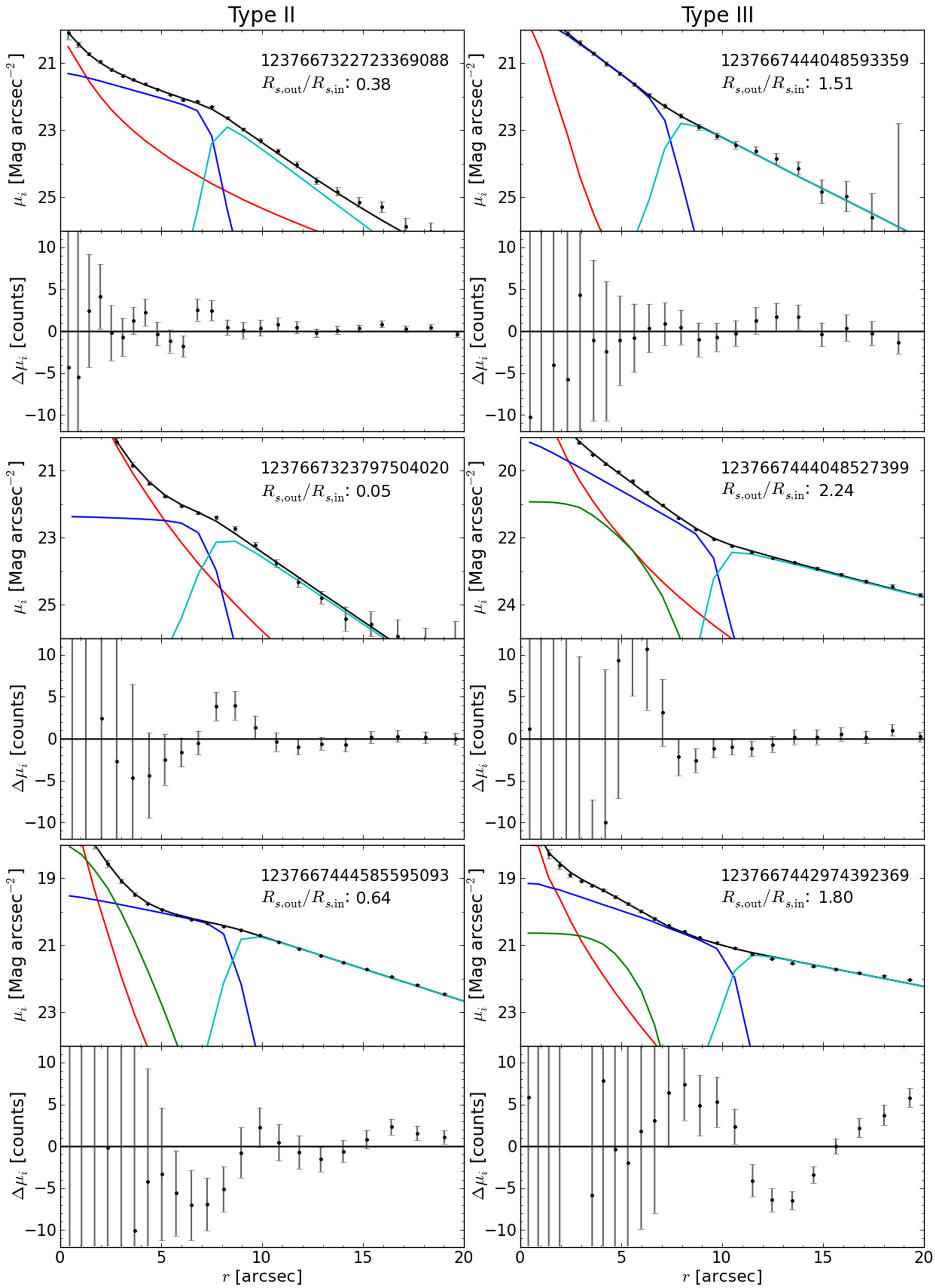

Figure 5. Example (major axis) surface brightness profiles for six galaxies (three *BDd*, three *BSDd*) best fitted by broken disc models (three Type II, three Type III). Upper panels: the *i*-band surface brightness as measured from the galaxy thumbnail (black points) in wedges of elliptical annuli. The corresponding model components are indicated as solid lines (black/red/green/blue/cyan: total/bulge/bar/inner disc/outer disc). Lower panels: model residual (in counts). Error bars in both plots (grey) are the standard error on the mean surface brightness in each wedge. All examples include the ratio of the outer and inner disc scalelengths ($R_{\mathrm{s,out}}/R_{\mathrm{s,in}}$).

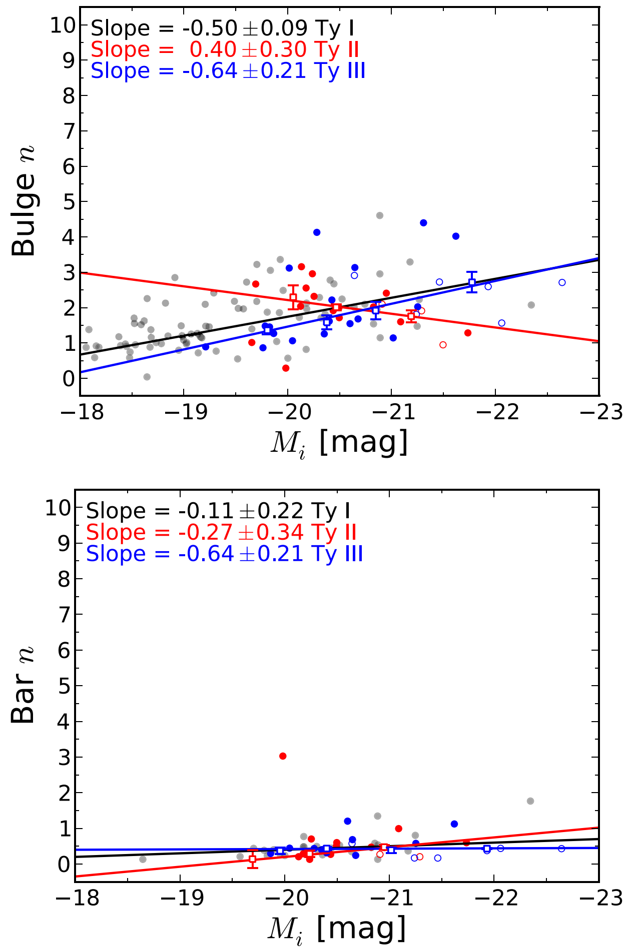

Figure 6. Bulge and bar Sérsic indices (n) for *BD*, *CD*, *BDd*, *CDd*, *BSD*, and *BSDd* model galaxies with Type I (black), II (red), and III (blue) discs as a function of total absolute i-band model magnitude. Upper plot: bulge Sérsic index. Lower plot: bar Sérsic index. Unfilled data points indicate flagged galaxies. Large square points are median parameter values in bins of M_i, to which a linear trend has been fit. Type I galaxies are indicated by small grey points for clarity.

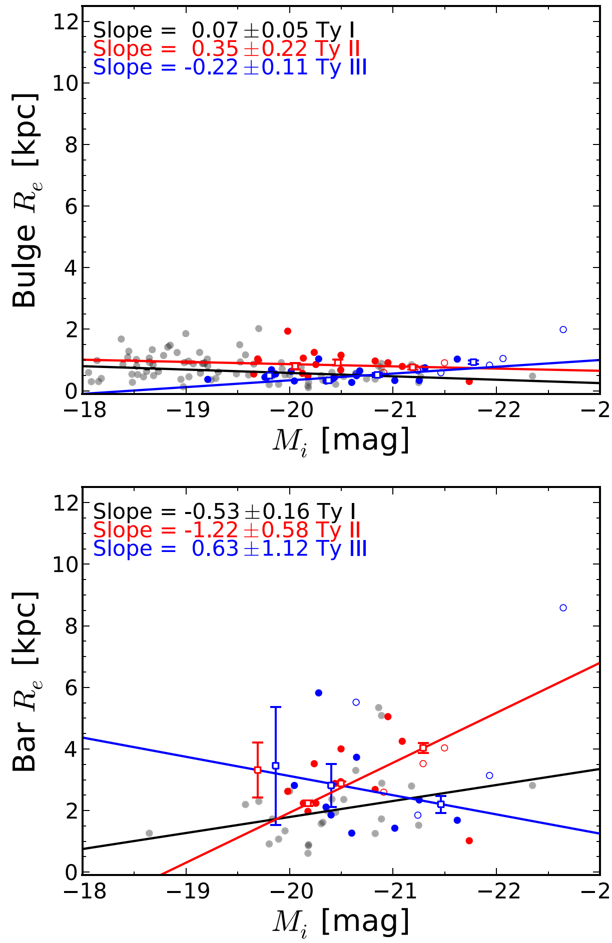

Figure 7. Bulge and bar effective half-light radii (R_e) for *BD*, *CD*, *BDd*, *CDd*, *BSD*, and *BSDd* model galaxies with Type I (black), II (red), and III (blue) discs as a function of total absolute i-band model magnitude. Upper plot: bulge R_e. Lower plot: bar R_e. Unfilled data points indicate flagged galaxies. Large square points are median parameter values in bins of M_i, to which a linear trend has been fit. Type I galaxies are indicated by small grey points for clarity.

magnitude range $-19 < M_i < -22$ for consistency with the range of Type II and III galaxy luminosities.

With increasing galaxy luminosity, no significant variation in bar n is detected for any galaxy type. However, the bulges of both Type I and Type III galaxies become more centrally concentrated (higher n) for more luminous galaxies. Similar n–M_i slopes are measured for both galaxy types (consistent with the equivalent trend measured previously for archetypal *BD* models in Paper I). The reverse trend (lower n for higher galaxy luminosity) is measured for Type II galaxies. While this trend is not significant ($\sim 1.5\sigma$), it remains discrepant with the measured Type I/III trends at a 3σ level. Thus, the bulges of galaxies with truncated discs are structurally distinct from those found in galaxies with untruncated, or antitruncated discs. This is analogous to the distinct n-luminosity trends measured in the previous section for barred and unbarred galaxies. However, as barred galaxies comprise approximately equal numbers of Type II (23^{+5}_{-4} per cent) and III discs (19 ± 4 per cent), this apparent bulge n bimodality is not strongly related to the presence of a bar component.

Half-light radii for the bulges and bars of Type I, II, and III galaxies are presented in Fig. 7. The bulges of Type I and III galaxies show no significant size difference on average (Type I: 0.57 ± 0.05 kpc, Type III: 0.54 ± 0.05 kpc), while Type II galaxies have systematically larger bulges (0.96 ± 0.07 kpc). No notable trends in bulge size with galaxy luminosity is noted for galaxies of any Freeman type.

The bars in Type II galaxies are systematically larger on average (2.91 ± 0.22 kpc) than those found in Type I galaxies (1.95 ± 0.18 kpc), but similar to the bars of Type III galaxies (2.82 ± 0.49 kpc). As with bulge components, no significant size–luminosity trends are noted for galaxy bars. Thus, large galaxy bars are found more frequently in galaxies with broken (truncated/antitruncated) discs, regardless of total galaxy luminosity.

In summary, the bulges of galaxies with Type II discs have systematically larger n and R_e than the bulges of Type I or III galaxies. In addition, no significant bulge n-luminosity trend is detected for Type II galaxies. Thus, the bulges of galaxies with truncated discs are distinct in structure and origin from the equivalent components in galaxies with either untruncated or antitruncated discs. Galaxy

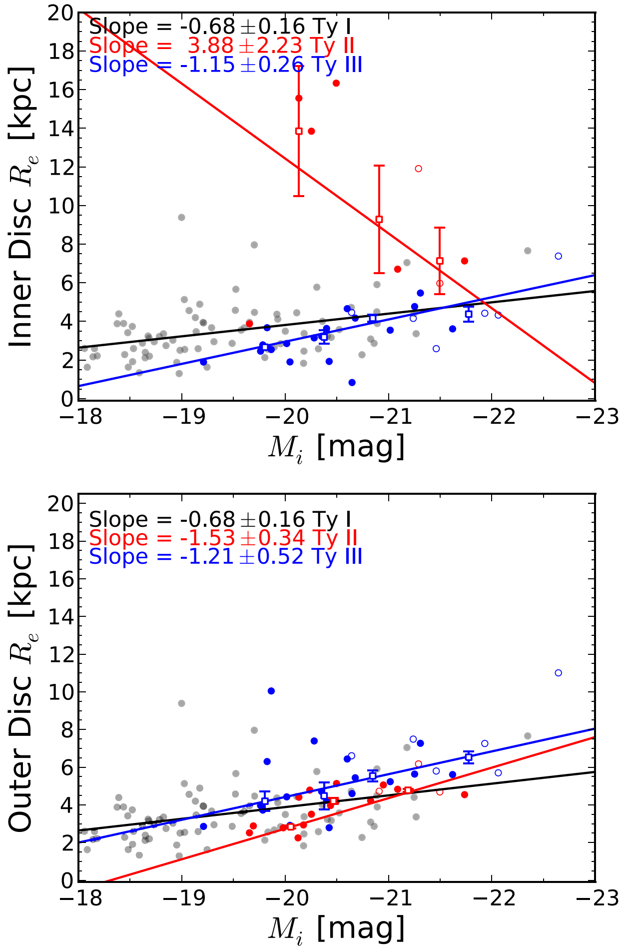

Figure 8. Inner and outer disc effective half-light radii (R_e) for *BD*, *CD*, *BDd*, *CDd*, *BSD*, and *BSDd* model galaxies with Type I (black), II (red), and III (blue) discs as a function of total absolute *i*-band model magnitude. Upper plot: inner disc R_e. Lower plot: outer disc R_e. Unfilled data points indicate flagged galaxies. Large square points are median parameter values in bins of M_i, to which a linear trend has been fit. Type I galaxies are indicated by small grey points for clarity.

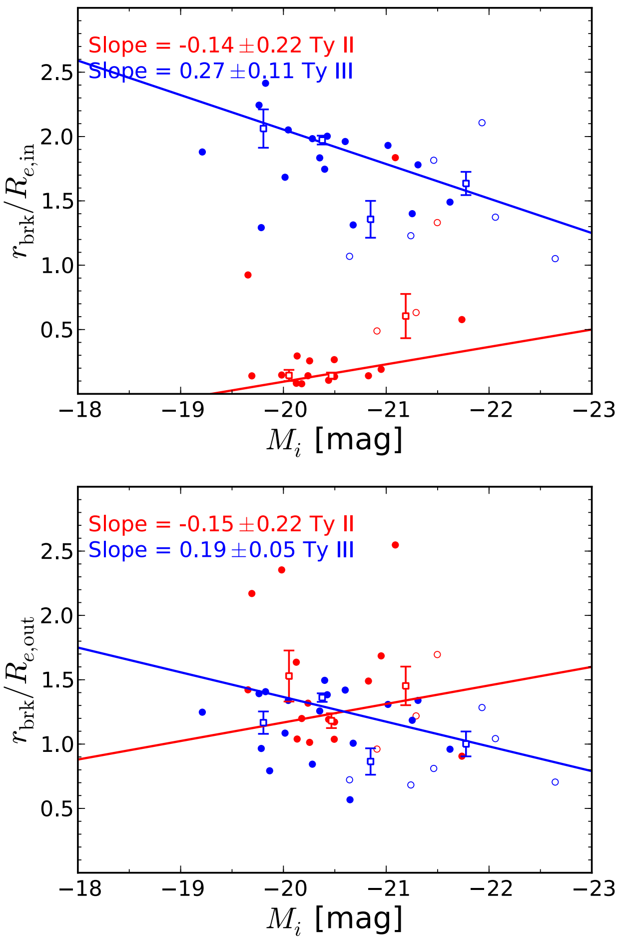

Figure 9. Break radius, $r_{\rm brk}$, as a function of the total absolute *i*-band model magnitude for galaxies with Type II (red) and III (blue) disc models relative to the inner (top) and outer (bottom) disc R_e. Unfilled data points indicate flagged galaxies. Large square points are median parameter values in bins of M_i, to which a linear trend has been fit.

bars are consistent in profile shape across all Freeman types, but have systematically larger R_e in galaxies with Type II or III broken discs.

4.4.2 *Type I/II/III disc properties*

The effective half-light radii for the inner and outer discs (i.e. the discs internal and external to the break radius, $r_{\rm brk}$) of Type II (truncated) and III (antitruncated) galaxies are presented in Fig. 8, with the disc R_e for Type I galaxies included in both panels. Note that by definition, the inner R_e of Type II/III galaxies is larger/smaller than the outer R_e, yielding a shallower disc surface brightness profile within/beyond $r_{\rm brk}$. On average, Type III inner discs are consistent in size (3.58 ± 0.20 kpc) with Type I discs (3.68 ± 0.18 kpc), and have a consistent size–luminosity relation (despite an $\sim 2\times$ difference in slope). By contrast, Type II inner discs are *substantially* larger (than Type I discs) on average (9.28 ± 1.44 kpc), with an extremely steep trend (4.76 ± 3.09 kpc per mag) of *decreasing* inner disc size with increasing galaxy luminosity, albeit at low significance ($\sim 1.5\sigma$).

The outer discs ofType II galaxies have scalelengths (4.12 ± 0.20 kpc) consistent with Type I discs (for galaxies in the range $-19 < M_i < -22$) on average, while Type III outer discs are systematically larger (5.62 ± 0.34 kpc). Outer disc size–luminosity relations are similar for both Type II and III discs, yielding size increases for more luminous galaxies a factor of approximately 2 times greater than the measured trend for Type I discs. However, this difference relative to Type I discs is only significant (at a $\sim 2.5\sigma$ level) for Type II galaxies. The detection of consistent scalelengths (and similar size–luminosity relations) for Type I discs, Type II outer discs, and Type III inner discs (in agreement with Laine et al. 2014) suggests that the outer/inner structures of Type II/III discs preserve the structural properties of their progenitor discs.

The break radius, $r_{\rm brk}$, is plotted in Fig. 9 for Type II and III discs as a fraction of both inner and outer disc R_e. For Type II discs, the break radius is a small fraction of the inner disc size (~ 0.25). However, since R_e is large for these structures, the contribution of the (flat) inner disc to the total disc luminosity is non-negligible. By comparison, Type III disc break radii are significantly beyond the inner disc half-light radius ($r_{\rm brk} \sim 2R_e$), indicating that only the outer wings of Type III inner disc structures are modified by the profile break. Alternatively, both Type II and III profile breaks are

Table 5. Table of best-fitting component light fraction–luminosity trends ($\Delta_{C/T}$; *C*/*T* per magnitude galaxy luminosity) measured for 2-component (top) and 3-component (bottom) galaxies. Here, a negative value indicates increasing *C*/*T* with luminosity.

		N	$\Delta_{B/T}$	$\Delta_{S/T}$	$\Delta_{D/T}$
2-comp.	Type I	56	-0.01 ± 0.03	–	0.01 ± 0.03
	Type II	4	-0.10 ± 3.65	–	0.10 ± 3.65
	Type III	7	-0.12 ± 0.11	–	0.12 ± 0.11
3-comp.	Type I	41	-0.04 ± 0.03	-0.10 ± 0.03	0.12 ± 0.04
	Type II	21	0.11 ± 0.07	0.01 ± 0.05	-0.22 ± 0.06
	Type III	17	-0.14 ± 0.02	0.07 ± 0.03	0.05 ± 0.03

comparable in size to the *outer* disc $R_{\rm e}$. Thus, in both cases, the outer structure of broken discs contribute ~50 per cent of the light of an equivalently sized untruncated disc.

In comparison to either disc, Type III breaks occur at smaller fractions of disc $R_{\rm e}$ for increasingly luminous galaxies. Note, however, that this correlation is significant at a $>3\sigma$ level for outer disc $R_{\rm e}$, but only significant at an $\sim 2.5\sigma$ level for inner disc $R_{\rm e}$. A decreased fractional break radius indicates that a Type III disc contains a smaller proportion of the primordial disc. Conversely, Type II break radii exhibit a non-significant increase (as fractions of both $R_{\rm e}$) with galaxy luminosity. Thus, the break radius of a Type II disc is approximately the same fraction of the inner/outer disc size for any galaxy. Note that if Type II discs where $R_{\rm e,in}$ reaches the GALFIT limit are excluded, the trend in $r_{\rm brk}$ relative to $R_{\rm e,out}$ is made considerably shallower. Hence, $r_{\rm brk}$ increases in size at a similar rate to outer disc $R_{\rm e}$ with total galaxy luminosity.

In summary, the inner discs of antitruncated (Type III) galaxies are consistent in size with the discs of unbroken (Type I) galaxies. Conversely, Type III outer discs are systematically larger than unbroken discs. Both inner and outer Type III discs exhibit a size–luminosity relation consistent with Type I discs. Thus, the inner discs of Type III galaxies preserve the properties of the unbroken progenitor disc. The inner discs of truncated (Type II) galaxies are not consistent in size or size–luminosity trend with unbroken discs. This rules out a formation scenario in which physical truncation preserves the primordial disc within the break radius. Conversely, the outer discs of Type II galaxies have sizes (and size–luminosity relations) consistent with untruncated disc structures.

4.4.3 Component fractions (C/T) of Type I/II/III galaxies

In this section, we discuss the component flux fractions (*B*/*T*, *S*/*T*, and *D*/*T* for bulges, bars, and discs, respectively) for galaxies with Type I, II, and III discs.

Measured across all (2- and 3-component) galaxies, Type I galaxies are strongly disc-dominated (median $D/T = 0.62 \pm 0.02$), with (subdominant) bulges ($B/T = 0.28 \pm 0.02$) and weak bar components ($S/T = 0.10 \pm 0.01$). The corresponding component fractions for Type III galaxies are measured to be consistent with Type I galaxies ($D/T = 0.62 \pm 0.03$, $B/T = 0.24 \pm 0.02$, $S/T = 0.14 \pm 0.03$). By contrast, Type II galaxies have a diminished disc light fraction on average ($D/T = 0.46 \pm 0.04$), with corresponding increases in bulge ($B/T = 0.33 \pm 0.04$) and bar ($S/T = 0.21 \pm 0.03$) fractions. Note, however, that these averages are heavily biased by the lack of a bar (i.e. $S/T = 0.00$) in 2-component galaxies. If the average is calculated from only 3-component galaxies, then bar light fraction (*S*/*T*) increases significantly for all three disc types (Type I: 0.24 ± 0.02; Type II: 0.25 ± 0.02; Type III: 0.20 ± 0.03). The corresponding disc light fractions (*D*/*T*) decrease on average for 3-component galaxies (Type I: 0.51 ± 0.03; Type II: 0.43 ± 0.04; Type III: 0.55 ± 0.03), while average bulge fractions (*B*/*T*) are not significantly changed (Type I: 0.25 ± 0.02; Type II: 0.31 ± 0.04; Type III: 0.20 ± 0.03).

The best-fitting component light fraction trends with galaxy luminosity (2-component and 3-component galaxies considered separately) are presented in Table 5. For 2-component galaxies, no significant trends are noted in Type I galaxy *B*/*T* or *D*/*T*, while no conclusions can be drawn for Type II and III galaxies due to small sample sizes. However, with increasing luminosity, 3-component Type I galaxies become significantly more bar-dominated (-0.10 ± 0.03), and less disc-dominated (0.12 ± 0.04). Conversely, 3-component Type II galaxy disc light fraction and Type III galaxy bulge light fraction increases with galaxy luminosity (-0.22 ± 0.06 and -0.14 ± 0.02, respectively).

These component light fraction–luminosity trends can be used to estimate whether the distinction between faint and bright galaxies is dominated by the luminosity difference of one particular component. This can characterize, for example, whether the difference between an average galaxy and an equivalent galaxy 1 mag brighter is primarily due to an increase in bulge or disc luminosity. Hence, we will determine whether the apparent differences in *C*/*T* trends between Freeman types corresponds to intrinsically different component light scaling relations.

For two galaxies separated in total galaxy luminosity by 1 mag ($M_0 - M = 1.0$), the fractional difference in the luminosity of a particular component (C) can be parametrized as $x_C = L_C/L_{C,0}$. For example, if the galaxy luminosity difference in Type I galaxies at $M_{i,0} = -20$ and $M_i = -21$ was caused by the bulge and disc components being three times brighter at $M_i = -21$ (but bars being as luminous in both cases), then $x_B = 3$, $x_S = 1$, and $x_D = 3$.

The reported *C*/*T* slopes ($\Delta_{C/T}$; Table 5) can be expressed as

$$\Delta_{C/T} = C_0/T_0 - C/T = C_0/T_0 \left(1 - \frac{x_C}{x_T}\right), \tag{2}$$

where fractional difference in total luminosity, $x_T = 2.5$ across 1 mag. Note that x_C/x_T is greater than unity if component luminosity increases at a greater rate than galaxy luminosity.

Table 6 presents x_C values relative to a galaxy of average luminosity and *C*/*T* (i.e. $C_0/T_0 = \langle C/T \rangle$). For a galaxy brighter than the average by an arbitrary magnitude difference ($M_{\rm tot} = M_{\rm tot,0} + \Delta M_{\rm tot}$), the proportion of the total luminosity difference ($\Delta L_{\rm tot}$; where $L_{\rm tot,0} = L_{\rm tot} + \Delta L_{\rm tot}$) attributed to each photometric component (ΔL_C) can be estimated using:

$$\frac{\Delta L_C}{\Delta L_{\rm tot}} = C/T\,\frac{(x_T - 1) - x_T\,\Delta_{C/T}}{x_T - 1}. \tag{3}$$

Table 6. Table of approximate fractional component luminosity changes for 3-component Type I, II, and III galaxies as total galaxy luminosity increases ($x_T = 2.5$).

	N	x_B/x_T	x_S/x_T	x_D/x_T
Type I	41	1.16 ± 0.12	1.41 ± 0.13	0.76 ± 0.08
Type II	21	0.65 ± 0.23	0.96 ± 0.20	1.51 ± 0.15
Type III	17	1.56 ± 0.09	0.66 ± 0.16	0.91 ± 0.06

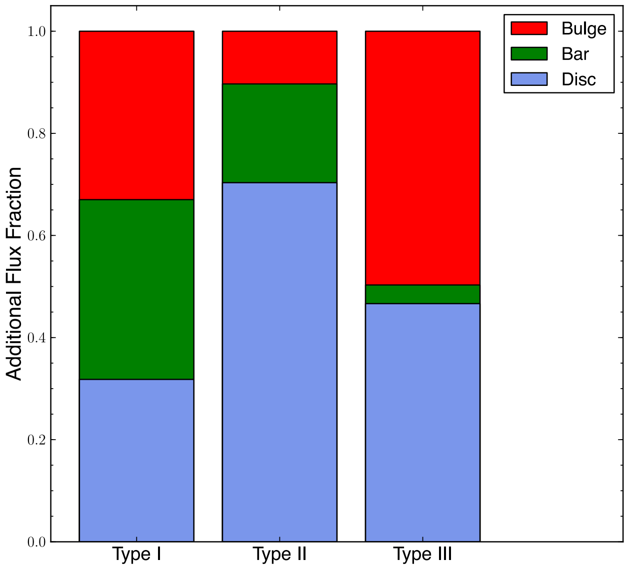

Figure 10. 'Additional' component light fractions (i.e. the proportions of the luminosity difference for each component structure per unit galaxy luminosity) for average galaxies with Freeman Type I, II and III disc components. Indicates the fraction of light added to the bulge (red), disc (blue) or bar (green) per unit of increased galaxy luminosity. Type I galaxies – bulge: 33 ± 3 per cent, disc: 35 ± 3 per cent, bar: 32 ± 4 per cent; Type II galaxies – bulge: 10 ± 2 per cent, bar: 19 ± 2 per cent, disc: 70 ± 12 per cent; Type III galaxies – bulge: 50 ± 4 per cent, bar: 4 ± 1 per cent, disc: 47 ± 6 per cent.

The resulting component fractions of the additional galaxy luminosity is illustrated in Fig. 10 for Type I, II and III galaxies.

For Type I galaxies, bars become more luminous at a significantly greater rate than the overall galaxy luminosity (bar luminosity doubles for a 42 per cent increase in total luminosity), while discs increase in luminosity at a slower rate (52 per cent increase in disc luminosity as galaxy luminosity doubles). However, the luminosity difference for Type I galaxies arbitrarily brighter than the average is distributed equally between all three structural components (from equation 3; Fig. 10). For example, an average Type I galaxy ($\langle M_i \rangle = -20.3$) has a total luminosity of 8.6×10^9 L$_\odot$. Relative to this average, a 9.6×10^9 L$_\odot$ Type I galaxy (i.e. 10^9 L$_\odot$ brighter) would have a bulge more luminous by $(3.3 \pm 0.4) \times 10^8$ L$_\odot$, a bar more luminous by $(3.5 \pm 0.3) \times 10^8$ L$_\odot$, and a disc $(3.2 \pm 0.4) \times 10^8$ L$_\odot$ more luminous.

For Type II galaxies, the disc component is the dominant contribution to luminosity growth (70 ± 12 per cent of $\Delta L_{\rm tot}$), doubling in luminosity for each 32 per cent increase in galaxy luminosity. Hence, the disc-total luminosity trend is significantly steeper for Type II discs than Type I, indicating a larger difference in disc luminosity between faint and bright Type II galaxies than for Type I galaxies. This implies that fainter Type II galaxies have experienced a greater truncation (of light) than intrinsically more luminous galaxies.

For Type III galaxies, the bulge is the dominant component (doubling in luminosity for a 28 per cent increase in global luminosity). For an average Type III galaxy, the bulge component's contribution to galaxy luminosity is approximately equal to the (intrinsically more luminous) disc. The corresponding bar light contribution is minimal (3.7 ± 0.4 per cent of $\Delta L_{\rm tot}$), indicating approximately equally luminous bars in all Type III galaxies, independent of total galaxy luminosity.

No other components (bulges in Type I galaxies, bulges and bars in Type II galaxies, and bars and discs in Type III galaxies) differ significantly from increasing in luminosity proportional to the galaxy ($x_C \sim 1$). Note that since $x_T = 2.5$, no component in Type I, II, or III galaxies decreases in luminosity in brighter galaxies.

In summary, 3-component archetypal (central bulge + outer-dominant disc + any bar) galaxies are disc-dominated on average, with approximately equal bulge and bar light fractions, independent of Freeman disc/galaxy type. The measured trends in component light fraction with total magnitude were used to quantify the contributions of each structural component to galaxy luminosity. All three structural components contribute equally on average to the increasing total luminosity in galaxies unbroken discs (Type I). However, the bar component exhibits the largest fractional increase in luminosity. Discs were found to dominate truncated (Type II) galaxy luminosities. The corresponding disc-total luminosity trend is steeper than for Type I galaxies, which may indicate disc (luminosity) truncation. Increasing antitruncated disc (Type III) galaxy luminosities correlate strongly with both their bulges and discs. Hence, bar luminosity in Type III galaxies is independent of galaxy luminosity.

4.5 Structural trends with environment

In this section, we investigate variation in the multicomponent structures of galaxies as a function of the (projected) distance from the Coma Cluster centre, $r_{\rm cluster}$. Observed $r_{\rm cluster}$ correlates with the time at which a galaxy first entered the cluster environment (Gao et al. 2004; De Lucia et al. 2012; Smith et al. 2012; Taranu et al. 2014), albeit with substantial scatter. A cluster-centric radial analysis therefore highlights the environment-mediated processes that have acted on these multicomponent systems, and hence the cluster environment's role in their formation.

The morphological mix of galaxies varies with position in the cluster (Fig. 11). Neither the fraction of multi-Sérsic models, nor the fraction of galaxies with broken discs vary significantly with cluster-centric radius. Note that, this would not change if Type II and III galaxies were considered separately (see Section 4.3). The fraction of pure Sérsic systems increases towards the cluster centre, while the fraction of (exponential) outer disc galaxies decreases. However, neither of these radial morphology trends are significant.

With increasing distance from the cluster centre, no significant variation ($>3\sigma$) is detected in the structural properties of Type I, II, or II galaxies. However, weakly significant radial trends ($\sim 2\sigma$) are detected in (barred) Type I galaxy bar size ($R_{\rm e}$; 1.3 ± 0.6 kpc per r_{200}), Type II outer disc size ($R_{\rm e,out}$; -1.5 ± 0.8 kpc per r_{200}),[6] and Type III galaxy bulge profile (n; 0.9 ± 0.5 per r_{200}). Thus, the

[6] Note that the sign of this trend indicates *increasing* outer disc size towards the cluster centre, and hence does not correspond to environmental truncation.

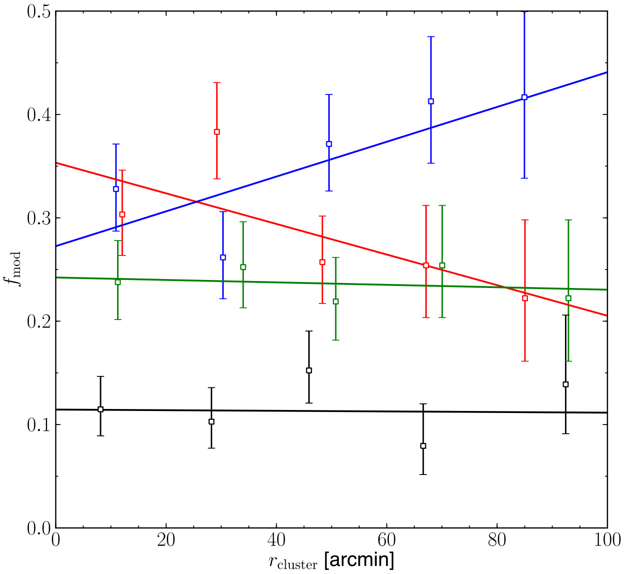

Figure 11. The model fractions, $f_{\rm mod}$ (i.e. number of each model type ÷ total number of galaxies per bin) as a function of radial position in the Coma Cluster, $r_{\rm cluster}$. Single Sérsic objects (*S*) are plotted in red, galaxies with outer exponential discs (*BD, CD, BSD*) are plotted in blue, galaxies with broken discs (*BDd, BSDd*) are plotted in black, and multi-Sérsic systems (*BS, BSS*) are plotted in green.

structural properties of galaxies with disc-dominated outer regions are independent of their radial position in the cluster. Therefore, the formation of disc breaks may result from secular, rather than environment-mediated processes.

5 DISCUSSION: DISC BREAK FORMATION SCENARIOS

Here, we briefly investigate the evolutionary origins of archetypal broken disc (truncated/antitruncated; Freeman Type II/III) galaxies through comparison of their structural and component photometric properties to unbroken (Type I) galaxies. As a working hypothesis, we assume a break formation scenario in which Type II and III galaxies had Type I discs at some point in the past. While the observed *present-day* Type I discs are not necessarily the progenitors of present-day broken discs, all three Freeman type galaxies are assumed to have evolved from a common population of primordial galaxies with (Type I) discs. Thus, characteristics of the structural/photometric distributions unique to galaxies of a particular Freeman type can be used to constrain their evolutionary pathways.

The absence of any strong cluster-radial trends in galaxy structure disfavours a (cluster) environment-driven origin for disc breaks. Furthermore, bar structures appear to be strongly related to the formation of Type II and III discs: while one half of all Type I galaxies contain a bar (42^{+5}_{-5} per cent barred, 58^{+5}_{-5} per cent unbarred), the bar fraction is considerably higher for Type II (89^{+5}_{-9} per cent) and Type III (71^{+8}_{-10} per cent) galaxies. Galaxy bars are also significantly larger if their host galaxy has a truncated/antitruncated disc than if the galaxy disc remains unbroken. This implies that either the formation mechanism induces bar growth, or that bars stabilize discs during truncation/antitruncation, such that the detection of a disc break for bright galaxies is more likely if a bar is present.

The detection in galaxy simulations of inner (and outer) disc evolution with time (Debattista et al. 2006; Minchev et al. 2012) supports a scenario of stellar (or gas) redistribution. In particular, the radial angular momentum transfer mechanism proposed in Minchev et al. (2012) would explain the apparent importance of a bar component, as such a structure would induce significant gravitational torques in disc gas. The significant increase in bar size for more luminous Type II galaxies may therefore suggest a period of enhanced star formation in the bar due to gas inflows, or the migration of disc stars into the bar.

Systematically larger Type II inner disc scalelengths (and inconsistent size–luminosity relations) compared to untruncated Type I galaxies indicates that the inner discs of Type II galaxies are not structures equivalent to Type I discs. This disfavours a scenario in which Type II discs represent a truncated system in which the outer disc is suppressed relative to the surviving primordial inner disc. Furthermore, while *D*/*T* is systematically lower in Type II galaxies compared to Type I, the fractional change in disc light does not differ significantly from unity ($x_D/x_T = 0.9 \pm 0.1$ as in equation 2, where x_T is the galaxy luminosity change between Type I and Type II galaxies). Hence, assuming an evolutionary scenario in which Type II galaxies evolve from Type I, disc luminosity increases proportional to the ~40 per cent increase in total galaxy luminosity (i.e. Type I: $m_T = 14.8 \pm 0.1$ versus Type II: $m_T = 14.5 \pm 0.1$). Intrinsically brighter Type II discs rule out a formation mechanism in which Type I discs are physical truncated. This conclusion is not compromised by the comparison of present-day truncated and untruncated discs unless evolution from primordial to present-day Type I galaxies also involves reduction of disc luminosity while preserving their untruncated profiles.

Beyond $r_{\rm brk}$, Type II discs represent structures reminiscent of their primordial Type I discs (see also Foyle, Courteau & Thacker 2008). Conversely, in the inner region ($r < r_{\rm brk}$) disc light has been redistributed such that the profile is flattened relative to a Type I profile. Bulges and bars in Type II galaxies are systematically larger than those in untruncated galaxies, implying that secular bulge/bar enhancement effects are significant for the formation of Type II galaxies. Thus, disc stars within $r_{\rm brk}$ may have been redistributed to form a bar and/or grow the galaxy bulge (see Valenzuela & Klypin 2003). Alternatively, the break formation mechanism may be enhanced via interaction with an existing bar, resulting in steeper inner/outer disc size trends with luminosity due to the strong bar size–galaxy luminosity relation.

Consistency in component scalelengths (and size–luminosity trends) between Type III and Type I galaxies implies that the Type III inner discs may correspond to undisturbed primordial (Type I) discs. Conversely, the (significantly larger) outer disc may represent an additional extended structure. Nevertheless, this outer structure maintains a disc-like size–luminosity relation. An evolutionary scenario from Type I (or Type I *progenitors*) to Type III is supported by the consistent bulge and disc component light fractions for both disc types, despite Type III galaxies being a factor of 1.9 times brighter on average. Hence, bulge and disc luminosities increase proportional to the galaxy luminosity difference between Type I and III galaxies.

Bulge and bar sizes in antitruncated galaxies are significantly larger than those in Type I galaxies, while bulge luminosity increases strongly in more luminous Type III galaxies ($x_B = 1.5x_T$; see Table 6). Thus, similar to Type IIs, the formation of Type III galaxies involves bulge/bar enhancement. However, unlike Type II discs, inner antitruncated discs do not appear to be structurally disturbed relative to Type I discs. Therefore, the additional bulge and outer disc light does not appear to result from restructuring of inner disc stars.

The transfer of angular momentum from a bar structure into the disc would cause an increase in disc scalelength outside a break radius (i.e. outer disc stars are redistributed to higher radii; Minchev et al. 2012). However, this mechanism does not explain the intrinsic *increase* in disc luminosity relative to Type I discs. Instead, it would be necessary to invoke additional star formation to build this additional stellar mass. If the progenitor disc was gas rich, outward angular momentum transfer from the bar could lead to an increased gas density at larger radii, and hence yield heightened star formation in the outer disc. Additionally, if disc gas *within* the break radius was simultaneously driven inwards by the bar, then the resulting central burst of star formation could explain the increased bulge luminosity. Central or outer starburst scenarios would be easily confirmed via the optical colours of these structural components (i.e. systematically bluer, indicating recent star formation). However, such a multiband analysis is beyond the scope of this work.

If secular angular momentum transfer due to bar components is the primary mechanism of disc break formation, then the distinction between Type II and III galaxies may be due to the absence/presence of cold gas in the progenitor disc: a gasless (i.e. quenched) progenitor would result in the redistribution of disc stars, and hence form a Type II disc, while the bar in a gas-rich progenitor may interact primarily with gas, yielding a Type III disc.

Alternatively, antitruncated disc formation scenario via merger events has been proposed in Borlaff et al. (2014). Such a merger event would add mass (≡luminosity) to the galaxy, and would grow the bulge component ($\propto M^{1-2}$; Boylan-Kolchin, Ma & Quataert 2005; van Dokkum et al. 2010; Hilz et al. 2012). In this paradigm, the outer Type III disc corresponds to a merger remnant structure, while the inner disc represents the surviving progenitor disc (potentially stabilized by the presence of a bar). If brighter galaxies assembled more mass via mergers, then the observation of decreasing $r_{\rm brk}/R_{\rm e,in}$ with increasing Type III galaxy luminosity can be understood as a decreasing fraction of the primordial disc surviving increasing mass ratio mergers.

6 SUMMARY AND CONCLUSIONS

In this paper, we have presented detailed decomposition analyses (both bulge–disc and more complex, multicomponent models) of ∼630 Coma Cluster galaxies (in the luminosity range $-17 > M_{\rm g} > -22$) using CFHT *i*-band imaging data. As this data is $\gtrsim$12 times deeper than SDSS, fitting accuracy and reliability was substantially improved relative to studies based on SDSS imaging data. This work focused on ETGs (notably those with outer discs, i.e. S0s).

The Sérsic bulge + exponential disc decomposition analysis previously presented in 'Paper I' has been extended to a wider range of candidate models including 3-component and/or broken disc models. This has allowed a detailed re-investigation of the ∼400 Coma Cluster galaxies previously considered to be poorly described by an archetypal (central) bulge + (outer) disc morphology, in addition to the ∼200 archetypal S0s in Paper I's analysis sample.

Rigorous model selection testing was implemented to ensure no dissonance exists between galaxy and (best-fitting) model structure. We have investigated the structural properties beyond the simple bulge + (exponential) disc morphology, the multicomponent structure of classic ellipticals, and the role of galaxy bars in the evolution of disc-dominated galaxies. Furthermore, the properties of broken disc structures (Freeman Types II and III) have been contrasted with the previously considered (unbroken) exponential disc (Freeman Type I), allowing investigation of the formation mechanisms (and hence evolutionary history) of galaxies containing such structures.

The key conclusions drawn from our analysis sample of 478 reliably fit Coma galaxies are as follows.

(i) 48 ± 3 per cent of galaxies ($N = 230$) are well described by a simple Sérsic, or Sérsic + exponential model, while 3(+) component models are required to describe 42 ± 3 per cent of galaxies ($N = 201$). Hence, a wide range of complex structures are found for ETGs in Coma.

(ii) Disc breaks are detected in 26 ± 4 per cent of archetypal (central bulge + outer disc) galaxies, with equal numbers of truncated (Freeman Type II; 12^{+3}_{-2} per cent) and antitruncated (Freeman Type III; 13^{+3}_{-2} per cent) discs. This corresponds to a significantly higher truncated disc fraction, and lower antitruncated disc fraction than has previously been detected for Virgo cluster galaxies.

(iii) Multicomponent Sérsic galaxies were resolved into a compact core (with $n \sim 2$), surrounded by large Gaussian-like structures. The total (combined) half-light radii for these multicomponent Sérsic galaxies are typically ∼11 kpc. Thus, if these galaxies formed from the compact 'red nuggets' detected at high redshifts, then these objects require a factor of ∼6 times growth in size.

(iv) No significant variation in galaxy morphology or multicomponent structure was detected with projected distance from the Coma Cluster centre. Therefore, secular processes are responsible for the *structural* changes responsible for the formation of broken disc galaxies.

(v) Disc breaks are found overwhelmingly in barred galaxies (Type II: 89^{+5}_{-9} per cent contain bars; Type III: 71^{+8}_{-10} per cent contain bars), while the minority of galaxies with unbroken discs also contain bars (42 ± 5 per cent). In addition, broken discs (of both types) are structurally correlated with bar size. Galaxy bars therefore play an important role in the formation or stabilization of Type II and Type III broken discs.

(vi) Type II discs may not be physically truncated. Rather, inner disc surface brightness may be suppressed in these structures, while the outer disc approximately preserves the progenitor disc properties. However, Type II disc luminosity trends are steeper than untruncated discs, suggesting luminosity truncation in fainter galaxies.

(vii) Significant growth of bulge size and luminosity implies a bulge enhancement origin (e.g. mergers, starbursts) for Type III galaxies, while the inner disc ($r < r_{\rm brk}$) remains structurally consistent with that of untruncated galaxies. Thus, 'antitruncated' discs are likely to result from either radial redistribution of disc gas due to bars, or (disc-preserving) merger events.

Model selection techniques are biased by the assumption that the set of considered models contains the 'true' representation of the underlying data. Here, the detection of genuine broken disc galaxies would have been significantly distorted if only a narrow a range of models are considered. False positive broken disc detection (i.e. the fraction of reported 'broken disc' galaxies revealed to have more complex, *unbroken* structures via a more detailed analysis) can exceed 50 per cent if 3-component and/or multi-Sérsic models are not also considered. Thus, decomposition analyses require a sufficiently broad range of candidate models in order to ensure meaningful results. Accordingly, consideration of models including more varied structural components (e.g. Ferrer bars, core-Sérsic bulges; Graham et al. 2003) may provide additional insight into the galaxies analysed in this work. However, this does not compromise the results of this study, which has explored the diversity of galaxy structures via the best fits *from the considered range of models*.

ACKNOWLEDGEMENTS

We thank Russell Smith for helpful discussion during the development of this paper. JTCGH was supported by an STFC studentship (ST/I505656/1). JRL is supported by STFC Rolling Grant ST/I001573/1. MJH acknowledges support from NSERC (Canada).

This work is based on observations obtained with MegaPrime/MegaCam, a joint project of CFHT and CEA/DAPNIA, at the Canada–France–Hawaii Telescope (CFHT) which is operated by the National Research Council (NRC) of Canada, the Institute National des Sciences de l'Univers of the Centre National de la Recherche Scientifique of France, and the University of Hawaii. This work is based in part on data products produced at TERAPIX with the expert assistance of Partick Hudelot and Yannick Mellier. Observational data used in this paper are available from the CFHT archive http://www3.cadc-ccda.hia-iha.nrc-cnrc.gc.ca/cfht/cfht.html.

This work uses data from SDSS-III. Funding for SDSS-III has been provided by the Alfred P. Sloan Foundation, the Participating Institutions, the National Science Foundation, and the US Department of Energy Office of Science. The SDSS-III web site is http://www.sdss3.org/.

SDSS-III is managed by the Astrophysical Research Consortium for the Participating Institutions of the SDSS-III Collaboration including the University of Arizona, the Brazilian Participation Group, Brookhaven National Laboratory, Carnegie Mellon University, University of Florida, the French Participation Group, the German Participation Group, Harvard University, the Instituto de Astrofisica de Canarias, the Michigan State/Notre Dame/JINA Participation Group, Johns Hopkins University, Lawrence Berkeley National Laboratory, Max Planck Institute for Astrophysics, Max Planck Institute for Extraterrestrial Physics, New Mexico State University, New York University, Ohio State University, Pennsylvania State University, University of Portsmouth, Princeton University, the Spanish Participation Group, University of Tokyo, University of Utah, Vanderbilt University, University of Virginia, University of Washington, and Yale University.

REFERENCES

Allen P. D., Driver S. P., Graham A. W., Cameron E., Liske J., de Propris R., 2006, MNRAS, 371, 2
Aragón-Salamanca A., 2008, in Bureau M., Athanassoula E., Barbuy B., eds, Proc. IAU Symp. 245, Formation and Evolution of Galaxy Bulges. Cambridge Univ. Press, Cambridge, p. 285
Barr J. M., Bedregal A. G., Aragón-Salamanca A., Merrifield M. R., Bamford S. P., 2007, A&A, 470, 173
Barway S., Wadadekar Y., Kembhavi A. K., Mayya Y. D., 2009, MNRAS, 394, 1991
Borlaff A. et al., 2014, A&A, 570, 103
Boselli A., Gavazzi G., 2006, PASP, 118, 517
Bower R. G., Lucey J. R., Ellis R. S., 1992, MNRAS, 254, 601
Boylan-Kolchin M., Ma C.-P., Quataert E., 2005, MNRAS, 362, 184
Capaccioli M., Vietri M., Held E. V., Lorenz H., 1991, ApJ, 371, 535
Cappellari M., 2013, ApJ, 778, L2
Cappellari M. et al., 2011, MNRAS, 416, 1680
Carter D. et al., 2008, ApJS, 176, 424
Chilingarian I. V., Zolotukhin I. Y., 2012, MNRAS, 419, 1727
Chilingarian I. V., Melchior A.-L., Zolotukhin I. Y., 2010, MNRAS, 405, 1409
Damjanov I. et al., 2009, ApJ, 695, 101
De Lucia G., Weinmann S., Poggianti B. M., Aragón-Salamanca A., Zaritsky D., 2012, MNRAS, 423, 1277
de Vaucouleurs G., 1948, Ann. Astrophys., 11, 247
Debattista V. P., Mayer L., Carollo C. M., Moore B., Wadsley J., Quinn T., 2006, ApJ, 645, 209
Dressler A., 1980, ApJ, 236, 351
Dressler A., Gunn J. E., 1983, ApJ, 270, 7
Driver S. P., Popescu C. C., Tuffs R. J., Liske J., Graham A. W., Allen P. D., de Propris R., 2007, MNRAS, 379, 1022
Dullo B. T., Graham A. W., 2014, MNRAS, 444, 2700
Eliche-Moral M. C., González-García A. C., Aguerri J. A. L., Gallego J., Zamorano J., Balcells M., Prieto M., 2013, A&A, 552, A67
Emsellem E. et al., 2011, MNRAS, 414, 888
Erwin P., Pohlen M., Beckman J. E., 2008, AJ, 135, 20
Erwin P., Gutiérrez L., Beckman J. E., 2012, ApJ, 744, L11
Foyle K., Courteau S., Thacker R. J., 2008, MNRAS, 386, 1821
Freeman K. C., 1970, ApJ, 160, 811
Gao L., De Lucia G., White S. D. M., Jenkins A., 2004, MNRAS, 352, L1
Gavazzi G., 1989, ApJ, 346, 59
Gavazzi R., Adami C., Durret F., Cuillandre J.-C., Ilbert O., Mazure A., Pelló R., Ulmer M. P., 2009, A&A, 498, L33
Gavazzi G., Fumagalli M., Cucciati O., Boselli A., 2010, A&A, 517, A73
Graham A. W., Erwin P., Trujillo I., Asensio Ramos A., 2003, AJ, 125, 2951
Guzman R., Lucey J. R., Carter D., Terlevich R. J., 1992, MNRAS, 257, 187
Häussler B. et al., 2007, ApJS, 172, 615
Head J. T. C. G., 2014, PhD thesis, Durham University
Head J. T. C. G., Lucey J. R., Hudson M. J., Smith R. J., 2014, MNRAS, 440, 1690 (Paper I)
Hilz M., Naab T., Ostriker J. P., Thomas J., Burkert A., Jesseit R., 2012, MNRAS, 425, 3119
Homeier N. L. et al., 2006, AJ, 131, 143
Huang S., Ho L. C., Peng C. Y., Li Z.-Y., Barth A. J., 2013, ApJ, 766, 47 (H13)
Hudson M. J., Stevenson J. B., Smith R. J., Wegner G. A., Lucey J. R., Simard L., 2010, MNRAS, 409, 405
Janz J. et al., 2012, ApJ, 745, L24
Janz J. et al., 2014, ApJ, 786, 105
Jørgensen I., 1999, MNRAS, 306, 607
Jørgensen I., Franx M., 1994, ApJ, 433, 553
Kaviraj S. et al., 2012, MNRAS, 423, 49
Kent S. M., 1985, ApJS, 59, 115
Komatsu E. et al., 2011, ApJS, 192, 18
Kormendy J., Bender R., 2012, ApJS, 198, 2
Laine J. et al., 2014, MNRAS, 441, 1992
Lansbury G. B., Lucey J. R., Smith R. J., 2014, MNRAS, 439, 1749
Laurikainen E., Salo H., Buta R., 2005, MNRAS, 362, 1319
Lucey J. R., Guzman R., Carter D., Terlevich R. J., 1991, MNRAS, 253, 584
Michard R., 1985, A&AS, 59, 205
Minchev I., Famaey B., Quillen A. C., Di Matteo P., Combes F., Vlajić M., Erwin P., Bland-Hawthorn J., 2012, A&A, 548, A126
Möllenhoff C., Popescu C. C., Tuffs R. J., 2006, A&A, 456, 941
Pastrav B. A., Popescu C. C., Tuffs R. J., Sansom A. E., 2013, A&A, 557, A137
Peng C. Y., Ho L. C., Impey C. D., Rix H., 2010, AJ, 139, 2097
Querejeta M., Eliche-Moral M. C., Tapia T., Borlaff A., Rodríguez-Pérez C., Zamorano J., Gallego J., 2015, A&A, 573, 78
Rawle T. D., Lucey J. R., Smith R. J., Head J. T. C. G., 2013, MNRAS, 433, 2667
Rix H.-W., White S. D. M., 1990, ApJ, 362, 52
Roediger J. C., Courteau S., Sánchez-Blázquez P., McDonald M., 2012, ApJ, 758, 41
Schlafly E. F., Finkbeiner D. P., 2011, ApJ, 737, 103
Schwarz G., 1978, Ann. Stat., 6, 461
Sérsic J. L., 1963, Bol. Asociacion Argentina Astron., 6, 41
Shapley H., 1934, Harv. Coll. Obs. Bull., 896, 3
Smith R. J., Lucey J. R., Hudson M. J., 2009, MNRAS, 400, 1690

Smith R. J., Lucey J. R., Price J., Hudson M. J., Phillipps S., 2012, MNRAS, 419, 3167
Struble M. F., Rood H. J., 1999, ApJS, 125, 35
Taranu D. S., Hudson M. J., Balogh M. L., Smith R. J., Power C., Oman K. A., Krane B., 2014, MNRAS, 440, 1934
Valenzuela O., Klypin A., 2003, MNRAS, 345, 406
van den Bergh S., 1976, ApJ, 206, 883
van den Bergh S., 1990, ApJ, 348, 57
van den Bergh S., 2009a, ApJ, 694, L120
van den Bergh S., 2009b, ApJ, 702, 1502
van Dokkum P. G. et al., 2010, ApJ, 709, 1018
van Dokkum P., Abraham R., Merritt A., Zhang J., Geha M., Conroy C., 2015, ApJ, 798, 45
van Dokkum P. G. et al., 2014, ApJ, 791, 45
Weinzirl T. et al., 2014, MNRAS, 441, 3083
Wolf M., 1902, Publ. Astrophys. Inst. Koenigstuhl-Heidelberg, 1, 125
Younger J. D., Cox T. J., Seth A. C., Hernquist L., 2007, ApJ, 670, 269

SUPPORTING INFORMATION

Additional Supporting Information may be found in the online version of this article:

Table C1. The structural and photometric parameters of multicomponent models fits (i band) for the entire galaxy sample. (http://mnras.oxfordjournals.org/lookup/suppl/doi:10.1093/mnras/stv1662/-/DC1).

Please note: Oxford University Press is not responsible for the content or functionality of any supporting materials supplied by the authors. Any queries (other than missing material) should be directed to the corresponding author for the paper.

APPENDIX A: MODEL TYPE EXAMPLES

Fig. A1 presents an illustrative example galaxy best fitted by a Sérsic-only model (upper panels), and the corresponding (overfit) bulge + disc model (lower panels). Surface brightness plots (μ_i) and model residuals (image − model in counts) are included for both model fits (top left), as measured from the galaxy and model thumbnails in wedges of elliptical annuli [angle $\cos^{-1}(e^2)$, where e is the eccentricity of the galaxy's target ellipse]. The i-band residual images (including only the central quarters) are presented in the bottom-right corners (black border) for each model fit. In addition, component residual images (i.e. the residual image after all model components *except* the target component are subtracted) are included along the bottom in panels bordered by their μ_i plot line colours (i.e. red and blue for Sérsic and exponential components, respectively). Here, the addition of a disc component improves the goodness of fit (lower χ^2_ν), but this improvement is not statistically significant given the increased number of fitting parameters (increased BIC).

Equivalent example plots for galaxies best fitted by all other model types (except *CD*, and *CDd* due to small sample sizes) are presented in Figs A2–A8. Each best-fitting model (upper panels) is compared to its next simplest equivalent model (in terms of number of model components; lower panels). Hence, best-fitting *BD* (Fig. A2) and *BS* (Fig. A3) models are compared to (underfit) *S* models; best-fitting *BDd* (Fig. A4), *BDD* (Fig. A5), *BSD* (Fig. A6), and *BSS* (Fig. A7) models are compared to (underfit) *BD* models; and the best-fitting *BSDd* model (Fig. A8) is compared to a (underfit) *BSD* model.

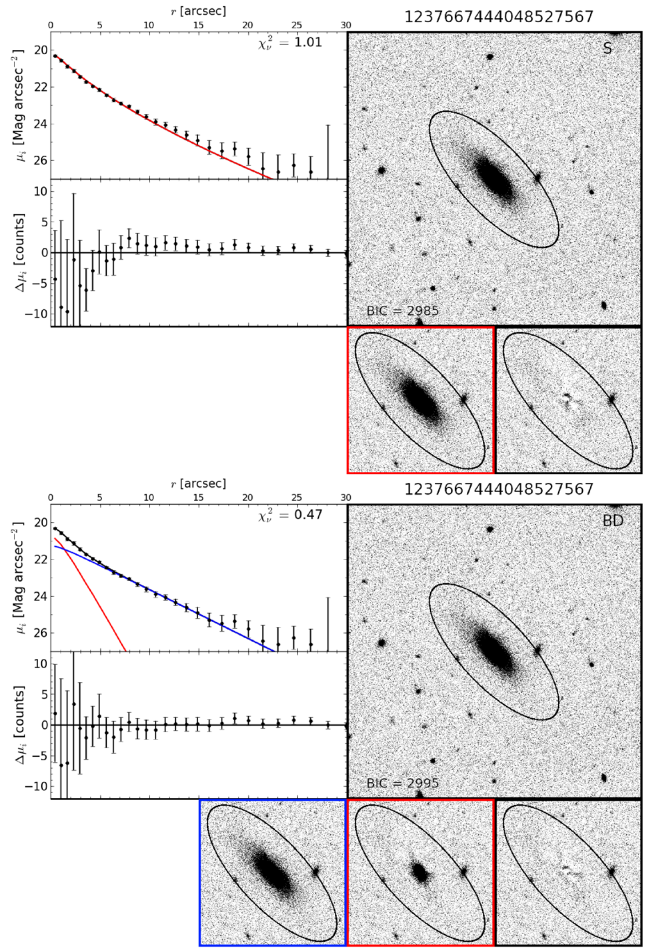

Figure A1. An example galaxy best fitted by an *S* model (DR8 ObjID 1237667444048527567): surface brightness profiles (μ_i), residuals ($\Delta\mu_i$), and i-band thumbnails for the *S* model (top: Sérsic = red), and the corresponding *BD* model (bottom: bulge = red, disc = blue). Small images depict isolated model components (border colours ≡ μ_i plot), and the total residual (black borders). The target ellipse is noted in black in all thumbnails, and 1D χ^2_ν (major axis) and 2D BIC values are included for both models.

APPENDIX B: DETAILS OF FITTING

B1 1D break parametrization

A simple 1D (outer) profile fitting procedure was used as a preliminary method of disc break detection. This was used primarily to produce realistic input parameter values for the 2D broken disc model fitting (see Section B4), but also identifies a sample of candidate broken disc galaxies.

Galaxy surface brightness profiles (as measured along the major axis in 45° wedges) were fit with a simple linear or broken linear model (analogous to exponential or broken exponential). Fitting was restricted to the range 3.54 arcsec $< r < r_{\rm sky}$ (where $r_{\rm sky}$ is the radius at which the total model surface brightness is equal to 4.94 times the sky uncertainty, following the methodology in Erwin et al. 2012) to avoid contamination of the surface brightness profile by the bulge or low-level sky background uncertainty. The inner limit (3.54 arcsec) comes from the radius at which the bulge contribution, $B/T(r)$, of an average archetypal galaxy (as determined in preceding chapters) drops below 1 per cent. The outer limit is increased relative to the

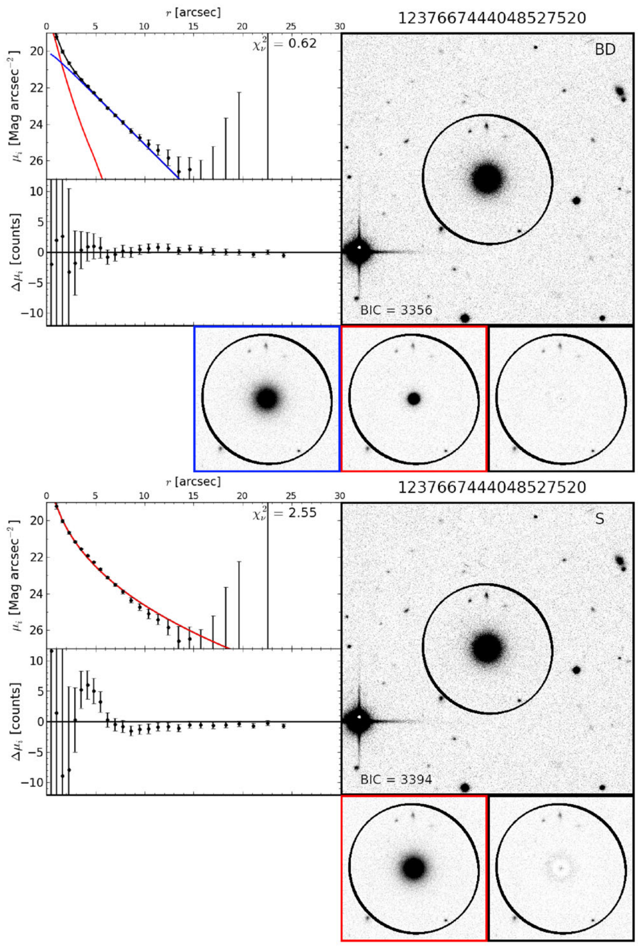

Figure A2. An example galaxy best fitted by a *BD* model (DR8 ObjID 1237667444048527520). As Fig. A1 for a *BD* model (top: bulge = red, disc = blue), and the corresponding *S* model (bottom: Sérsic = red).

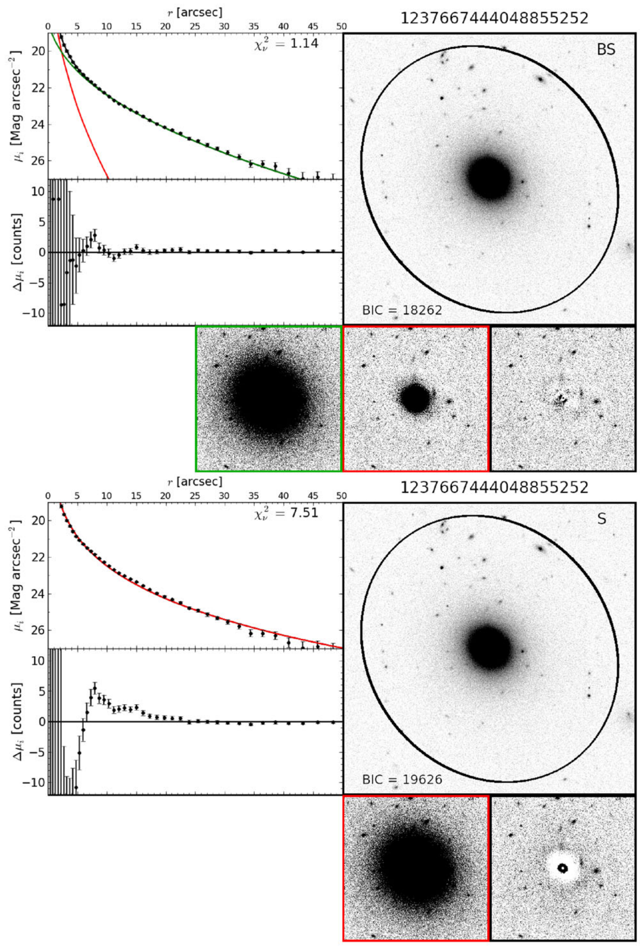

Figure A3. An example galaxy best fitted by a *BS* model (SDSS DR8 ObjID 1237667444048855252). As Fig. A1 for a *BS* model (top: bulge = red, Sérsic = green), and the corresponding *S* model (bottom: Sérsic = red).

analysis presented in previous chapters to allow the outer regions of galaxy surface brightness profiles to be characterized.

A 1D BIC was used to identify cases where the additional degrees of freedom afforded by the profile break significantly improved the model goodness-of-fit. For such broken galaxies, inner and outer disc scalelength values were calculated from the inner and outer slopes of the best-fitting broken linear models. The break radius was measured directly from the point at which the linear model switches from the inner to the outer slope.

Following 1D break detection, 215 galaxies (from an initial sample of 631 Coma Cluster galaxies) were selected as candidate broken discs. Subsequent analysis stages also include galaxies with no 1D-detected break; however, such galaxies must use generic input parameter values for broken disc model fitting.

B2 GALFIT

B2.1 Initial processing

To measure the structural and photometric parameters of galaxy bulges and discs, galaxy decomposition has been carried out using GALFIT (version 3.0.4), a 2D fitting routine (Peng et al. 2010). Given a user-specified model (of arbitrary complexity), GALFIT varies parameters based on a non-linear chi-squared minimization algorithm until no significant reduction in chi-squared (χ^2_ν) is found. The parameter values of this best-fitting 2-component model are used to estimate the underlying structure and photometry of the target galaxy.

For GALFIT's primary data input, ~100 arcsec × 100 arcsec thumbnail images were extracted from the MegaCam image frames, centred on each target galaxy. Secondary data products, as derived from the imaging data, were used to improve fitting robustness. These data products are described in detail in Paper I. This is given in brief as follows. The local background sky and the underlying statistical noise map were independently determined from each galaxy thumbnail. In addition, the image psf was characterized from stars in the MegaCam fields (no further than 5 arcmin from each galaxy), and the zero-point of the magnitude scale was calibrated using aperture photometry.

Absolute rest-frame magnitudes were calculated by subtracting the distance modulus ($m - M = 35.09$), and applying galactic dust extinction (using Schlafly & Finkbeiner 2011; 0.014 mag in the i band) and k-corrections (using Chilingarian, Melchior & Zolotukhin 2010; Chilingarian & Zolotukhin 2012; typically $\lesssim$0.01 mag).

B2.2 Initial conditions

For our analysis the initial conditions for the multicomponent fits are based on the best-fitting bulge + disc models presented in Paper I. The iterative build-up of model complexity from the

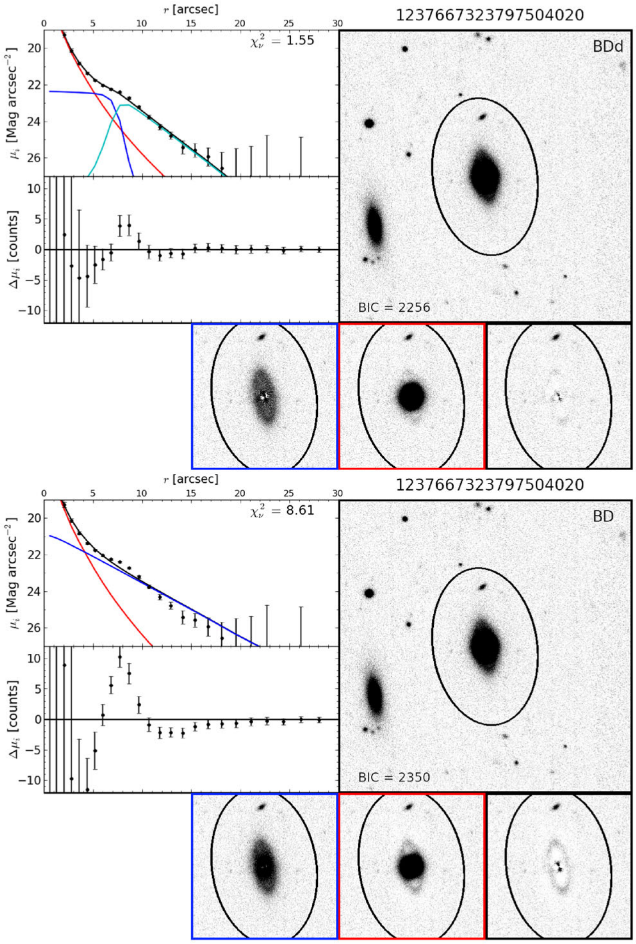

Figure A4. An example galaxy best fitted by a *BDd* model (SDSS DR8 ObjID 1237667323797504020). As Fig. A1 for a *BDd* model (top: bulge = red, inner/outer disc = blue/cyan), and the corresponding *BD* model (bottom: bulge = red, disc = blue).

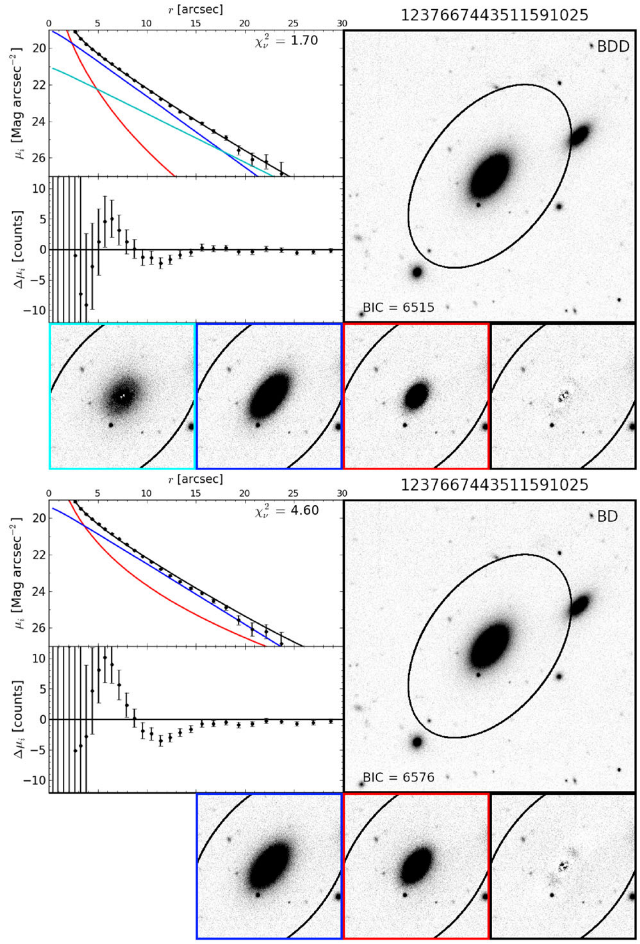

Figure A5. An example galaxy best fitted by a *BDD* model (SDSS DR8 ObjID 1237667443511591025). As Fig. A1 for a *BDD* model (top: bulge = red, disc1 = blue, disc2 = cyan), and the corresponding *BD* model (bottom: bulge = red, disc = blue).

best-fitting values of simpler models is the convention recommended for reliable results from GALFIT, and is used to provide a sensible starting point for the shapes (axial ratios), sizes, and intensity of additional model components. Hence, unlike Paper I, the model fitting procedure in this work was not extended (i.e. model parameters are not perturbed and refit to more thoroughly investigate the parameter space), as such an approach becomes computationally expensive (and highly sensitive to parameter degeneracies) for 3+ component models. Thus, the results of each input model were the product of one GALFIT cycle and instead care was taken to generate sensible initial parameter values. In addition to building model complexity iteratively, multiple input models were generated for a single model type if the prior model's components could be interpreted ambiguously. For example, a best-fitting *BD* model's bulge (or disc) structure can be used as the basis for the bulge, bar, or disc for an input *BSD* model. This build-up of model complexity is illustrated in Fig. B1.

B2.3 Parameter errors

While GALFIT provides an estimate of the parameter errors these are underestimate by a large factor (Häussler et al. 2007). The formal calculation of the parameter errors is both complex and very computationally expensive, and has not been carried out in this study. In our analysis in Section 4 where necessary we adopt the approach of using the scatter about the observed trends as an upper estimate of the statistical uncertainties in the parameters. For example, in Fig. 3 the observed scatter in the bulge Sérsic index found at each luminosity bin is ∼0.7 and hence if there is no intrinsic scatter this is a reasonable estimate of the Sérsic index error. In future work we will analyse mock images of galaxy with similar multicomponent structures found here in order to fully characterize the parameter uncertainties.

B2.4 Internal dust attenuation

In this paper we have not considered the possible effects of internal dust attenuation on the observed photometric structures. While this can bias measured structural parameters, particularly at bluer wavebands for spiral galaxies (Möllenhoff, Popescu & Tuffs 2006; Driver et al. 2007; Pastrav et al. 2013), over 90 per cent of our Coma sample are cluster ETGs where the dust content is likely to be small (Kaviraj et al. 2012). The $(B-R)$ colours of cluster red-sequence galaxies can be nearly fully accounted for by the observed spectroscopically determined stellar population trends to within an rms scatter of only ≃0.02 mag (Smith, Lucey & Hudson 2009). Such homogeneity in colour is unlikely to occur unless the internal extinction is uniformly small. Furthermore in our analysis highly inclined

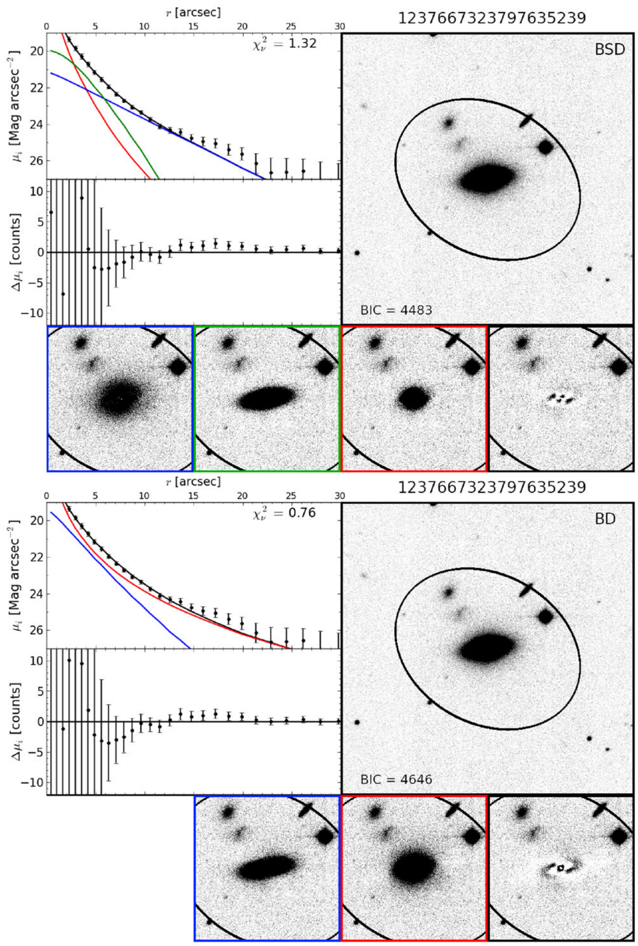

Figure A6. An example galaxy best fitted by a *BSD* model (SDSS DR8 ObjID 1237667323797635239). As Fig. A1 for a *BSD* model (top: bulge = red, bar = green, disc = blue), and the corresponding *BD* model (bottom: bulge = red, disc = blue).

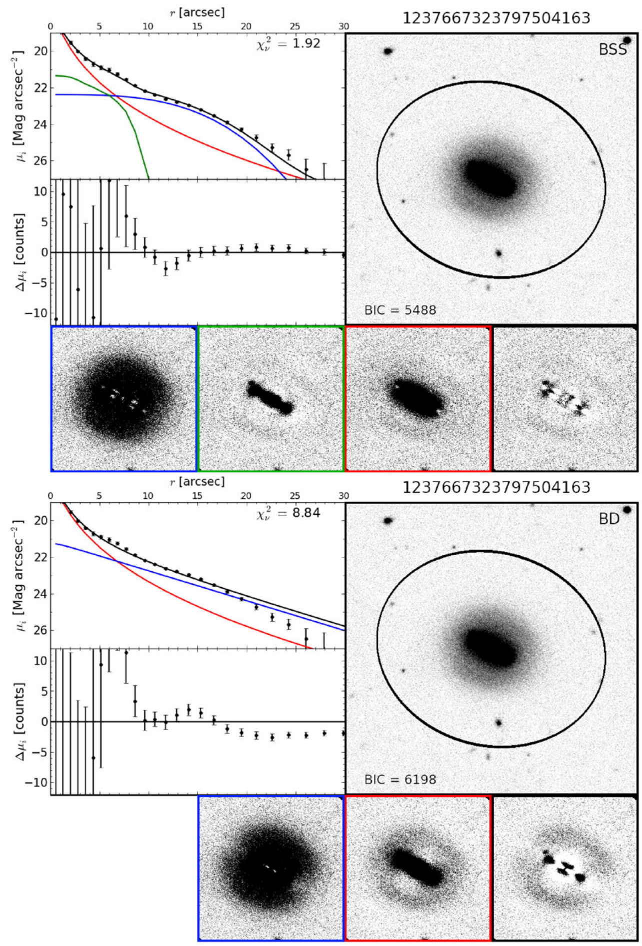

Figure A7. An example galaxy best fitted by a *BSS* model (SDSS DR8 ObjID 1237667323797504163). As Fig. A1 for a *BSS* model (top: bulge = red, Sérsic1 = green, Sérsic2 = blue), and the corresponding *BD* model (bottom: bulge = red, disc = blue).

galaxies, and those with strong dust lanes or strong asymmetries are excluded (see Section 3.2) in order to minimize the possible effects of dust on our conclusions.

B3 Surface brightness profile typing

For a multicomponent system, it is convenient to describe the combined model in terms of its component surface brightness profiles. Profile types for Sérsic + exponential models were first formalized in Allen et al. (2006) based on which component dominates at $r = 0$, and how many times the component profiles intersect (see Fig. B2). Type 1 profiles correspond to the archetypal central bulge + outer disc structure of spirals and S0s. Type 2/Type 5 profiles represent dominant discs/bulges at all radii, with subdominant bulges/discs. Conversely, the centrally dominant Sérsic component in Type 3 profiles redominates the model at large radii. These profiles may be non-physical representations of more complex (3+ component) systems. Profile Types 4 and 6 are equivalent to Types 1 and 3 with the roles of the Sérsic and exponential components swapped. As such, these inverted profiles may be symptoms of erroneous fitting pathways, rather than true physical structures.

B4 2D broken disc model

Fitting a broken disc structure requires a model profile with distinct inner and outer exponential scale radii, connected via a smooth transition. In GALFIT, this profile is implemented by linking two exponential disc profiles ($\Sigma_{\rm in}$ and $\Sigma_{\rm out}$) with (hyperbolic) truncation functions at some break radius. This (pixel surface brightness) profile can be expressed as

$$\Sigma(r) = T_1(r)\Sigma_{\rm in}(r) + T_2(r)\Sigma_{\rm out}(r), \tag{B1}$$

where T_1 and T_2 are the outer and inner truncation functions available for GALFIT (see Peng et al. 2010). The full functional form of the broken disc profile is

$$\Sigma(r) = \frac{1}{2}\left(1 - \tanh\left[(2-B)\frac{r}{r_{\rm brk}} + B\right]\right)\Sigma_{0,\rm in}\exp\left(\frac{-r}{R_{\rm s,in}}\right) + \frac{1}{2}\left(\tanh\left[(2-B)\frac{r}{r_{\rm brk}} + B\right] + 1\right)\Sigma_{0,\rm out}\exp\left(\frac{-r}{R_{\rm s,out}}\right), \tag{B2}$$

where $R_{\rm s,in}$ and $R_{\rm s,out}$ are the inner and outer disc scale radii, $\Sigma_{0,\rm in}$ and $\Sigma_{0,\rm out}$ are the (untruncated) central surface brightnesses of the inner and outer discs, and $r_{\rm brk}$ is the break radius. Here, $r_{\rm brk}$ is defined as the radius at which the inner and outer disc surface brightnesses are 1 and 99 per cent of their untruncated values,

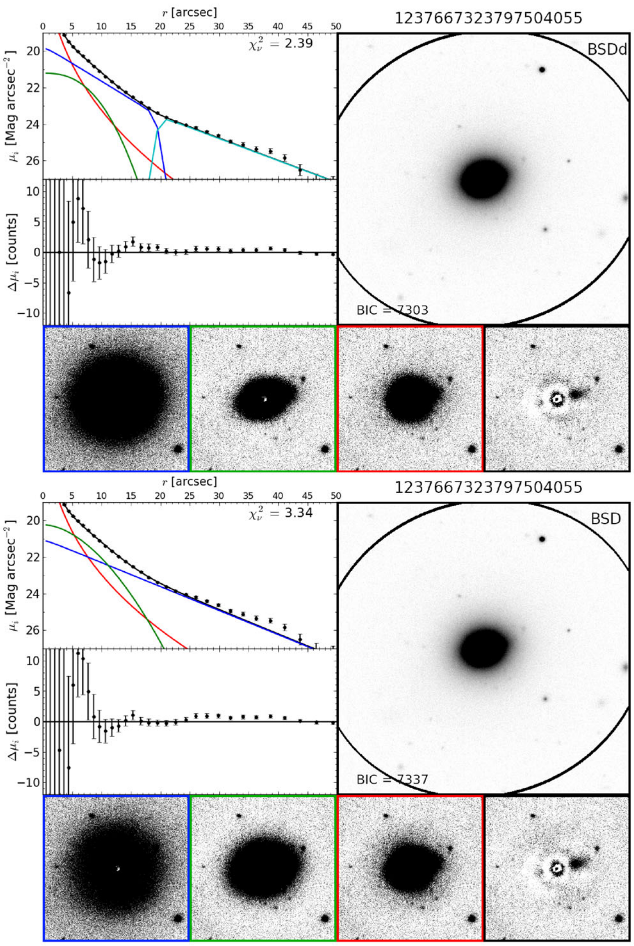

Figure A8. An example galaxy best fitted by a *BSDd* model (SDSS DR8 ObjID 1237667323797504055). As Fig. A1 for a *BSDd* model (top: bulge = red, bar = green, inner/outer disc = blue/cyan), and the corresponding *BSD* model (bottom: bulge = red, bar = green, disc = blue).

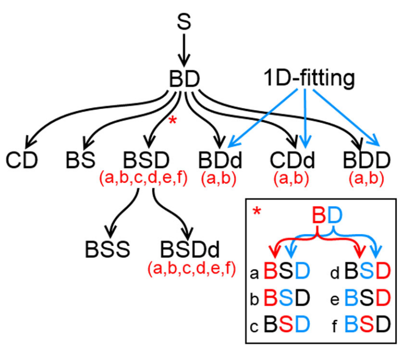

Figure B1. Graphical illustration of the relation between the models during multicomponent decomposition. Black arrows indicate which models take input parameter values from the best fit of a simpler model. Blue arrows indicate models which also take input parameter values from external sources. Models with multiple input variants (differing in their interpretation of progenitor model components) are noted in red. The inset illustrates multiple input generation for *BSD* models from the best-fitting *BD* components. 1D fitting is described in Appendix B1.

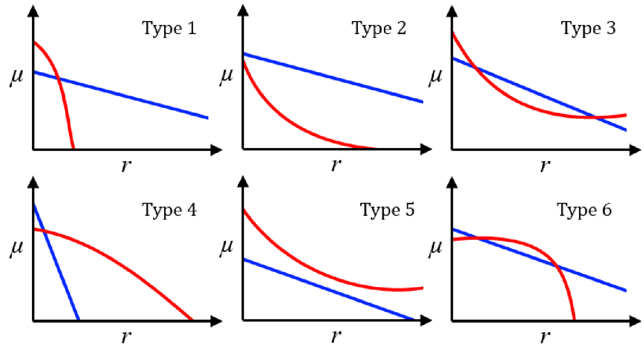

Figure B2. Cartoon surface brightness plots for Sérsic (red) + disc (blue) systems of each Allen type (Allen et al. 2006). Type 1 profiles are termed 'archetypal', while all other profiles are described as 'atypical'. Profile Types 4 and 6 are inversions of Types 1 and 3 (respectively), and may indicate erroneous fitting results.

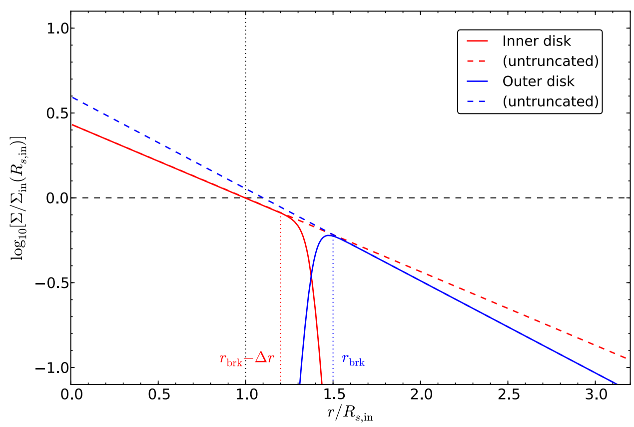

Figure B3. Cartoon example of the broken disc profile, indicating surface brightnesses of the inner (red) and outer (blue) discs (and their untruncated forms). r is normalized to the inner disc scalelength, $R_{\rm s,in}$ (black dotted line), and Σ is normalized to the inner disc surface brightness at $R_{\rm s,in}$ (black dashed line). The inner ($r_{\rm brk} - \Delta r$) and outer ($r_{\rm brk}$) truncation radii are indicated by red and blue dotted lines. In this example, $R_{\rm s,out} = 0.8R_{\rm s,in}$, $r_{\rm brk} = 1.5R_{\rm s,in}$, and $\Delta r = 0.3R_{\rm s,in}$.

respectively. Dimensionless parameter B is defined as $B = 2.65 - 4.98\left(\frac{r_{\rm brk}}{\Delta r}\right)$, where Δr is the break softening radius (radial difference within which the truncated flux drops from 99 to 1 per cent). An example of the broken disc profile is presented in Fig. B3 for a truncated (Type II) disc with a greatly exaggerated Δr.

The surface brightness of this model component can be fully described by a single GALFIT input parameter: surface brightness at the break radius, $\mu(r = r_{\rm brk})$. The value of $\mu(r = r_{\rm brk})$ is constrained to be identical for the inner and outer disc structures, ensuring continuity of the total component profile. Additionally, the axis ratios and PA parameters of both discs are coupled for structural consistency, and Δr is fixed at 0.1 pixel (0.02 arcsec). Hence, the broken disc profile includes only two more free fitting parameters ($R_{\rm s,out}$, and $r_{\rm brk}$; $k = 6$) than the usual exponential disc model ($k = 4$; see Table 2).

Fitting using a truncation function with GALFIT yields a component's surface brightness at $r_{\rm brk}$, rather than the total

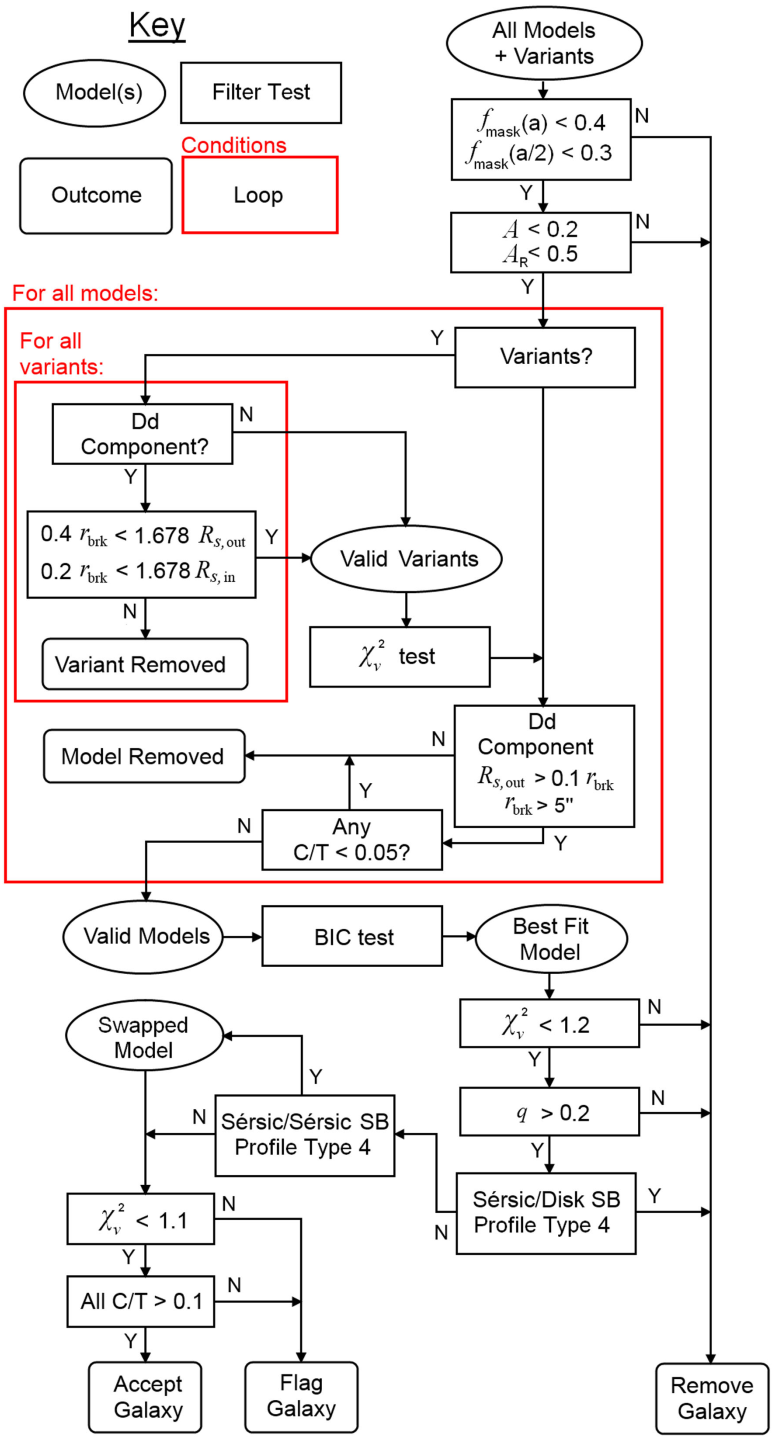

Figure B4. Flow chart illustrating multicomponent fitting model selection for models *S*, *BD*, *CD*, *BS*, *BDd*, *CDd*, *BDD*, *BSD*, *BSS*, and *BSDd*. For profile type definitions, refer to Section 3 and Allen et al. (2006).

component magnitude. Integrating equation (B2) to infinity, however, is non-trivial due to the tanh function. Instead the total broken disc profile luminosity can be approximated using

$$L_{\rm tot} = \int_0^{r_{\rm brk}} \Sigma_{\rm in}(r) 2\pi {\rm d}r + \int_{r_{\rm brk}}^{\infty} \Sigma_{\rm out}(r) 2\pi {\rm d}r, \tag{B3}$$

which approximates the truncation as a step function at $r_{\rm brk}$. The corresponding total profile magnitude is thus

$$m_{\rm tot} = m_{\rm zp} - 2.5\log_{10}[2\pi q] - 2.5\log_{10}\left[\Sigma_{0,\rm in} R_{\rm s,in}^2 \gamma\left(2, \frac{r_{\rm brk}}{R_{\rm s,in}}\right) + \Sigma_{0,\rm out} R_{\rm s,out}^2 \left(1 - \gamma(2, \frac{r_{\rm brk}}{R_{\rm s,out}})\right)\right], \tag{B4}$$

where q is the common disc axis ratio, and γ is the incomplete gamma function.

B5 Results filter

Results filtering is applied to ensure that only galaxies which can be reliably characterized by (one of) the smooth, symmetric candidate models are considered for analysis. Model selection (i.e. the identification of the most statistically meaningful candidate model) is also a key function of this filter. This process is based on the sample filtering in Paper I, which describes a number of test parameters in greater detail (notably A, $A_{\rm res}$, and $f_{\rm mask}$).

The filtering process for multicomponent fits is illustrated in Fig. B4, and summarized as follows:

(i) Galaxies are excluded if contaminated by nearby sources based on the number of masked galaxy thumbnail pixels within the target ellipse ($f_{\rm mask}(a_{\rm target}, q_{\rm target}) \geq 0.4$) and within the inner quarter of the target ellipse ($f_{\rm mask}(a_{\rm target}/2, q_{\rm target}) \geq 0.3$).

(ii) Asymmetrical galaxies are also removed ($A > 0.2$), but the threshold for removing galaxies based on *BD*-residual asymmetry was raised to $A_{\rm res} > 0.5$, as moderate residual asymmetry may simply indicate the presence of unfitted structural components.

(iii) For models with multiple variants (e.g. $BSD_{\rm a-f}$; see Fig. B1), a single (best-fitting) model is selected for analysis based on a simple χ^2 test. However, for models with broken discs (*BDd*, *CDd*, *BSDd*) model variants are excluded from consideration if $0.4r_{\rm brk} > 1.678R_{\rm s,out}$ (i.e. the outer disc contributes less than 8 per cent of its total flux) or $0.2r_{\rm brk} > 1.678R_{\rm s,in}$ (i.e. less than 0.3 per cent of the inner disc's total flux is truncated). These cuts remove anomalous model structures resulting from the broken disc component fitting to unintended structures.

(iv) For broken disc (*Dd*) models, galaxies are removed if $R_{\rm s,out} < 0.1r_{\rm brk}$ as a bug in GALFIT's truncation yields an additional (strong) central point source in this regime.

(v) Additionally, broken discs with $r_{\rm brk} < 5$ arcsec are removed, as the inner disc of such systems behave like point sources.

(vi) A BIC test (see equation 1) is applied to select the best-fitting model, which introduces the least extra fitting parameters. When comparing any two models, the least complex (lowest k) model is preferred unless the BIC value of the higher k model is at least $3\sigma_{\rm res}$ lower. For a range of (valid) candidate models, each model is paired and tested (in increasing order of complexity) with all other models until a best fit is found.

(vii) Models with (one or more) component-to-total ratios, $C/T<0.05$ are removed from consideration during the BIC test due to high parameter uncertainty. This is similar to the B/T cut for the selection of Sérsic-only models in Paper I, but does not make assumptions regarding the preferred 'simpler' model.

(viii) The χ^2_ν limit for (BIC-selected) models is lowered to $\chi^2_\nu > 1.2$, while galaxies are now flagged if $1.1 < \chi^2_\nu < 1.2$. This more critical cut in model χ^2_ν has been calibrated through visual examination of model residuals.

(ix) Galaxies with disc/outer component axis ratios, $q < 0.2$ are removed, as multicomponent decomposition cannot be meaningfully applied to edge-on systems.

(x) Models with Type 4 Sérsic/disc profiles (i.e. Type 4, *x*4*x*, *xx*4) are removed due to swapping of the bulge/bar and disc roles of the structural components.

(xi) Models with Type 4 Sérsic/Sérsic profiles (e.g. Type 4, 4*xx*) have their components swapped (e.g. bar and bulge swap) to maintain the 'inner' role of the bulge component (or 'inner'/'middle'/'outer' roles for components 1, 2, and 3 in *BSS* models). Galaxy models modified in this way are not removed or flagged.

(xii) Remaining models with $0.05 < C/T < 0.1$ are flagged as unreliable.

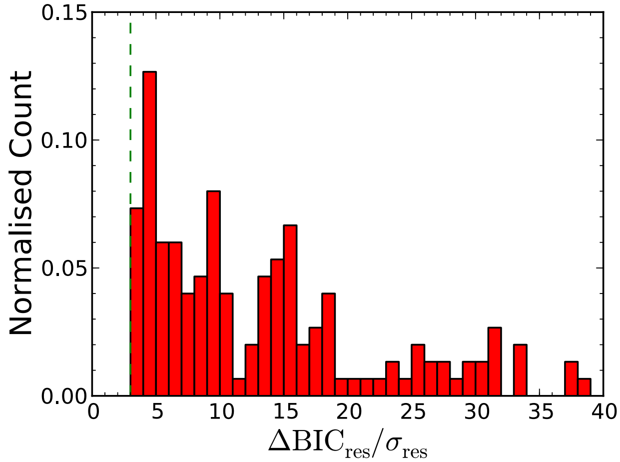

Figure B5. Histogram of ΔBIC$_{\rm res}$ values for well-fit, 2+ component models in the filtered sample ($N = 344$). This compares each best-fitting model to the next simplest (valid) model, plotted here relative to the uncertainty in ΔBIC$_{\rm res}$, $\sigma_{\rm res}$. A dashed green line is included to indicate the $3\sigma_{\rm res}$ cut-off for model acceptance.

B6 BIC test results

The results of the BIC test used to select the most statistically meaningful model for a given galaxy are illustrated in Fig. B5 for all multicomponent filtered sample galaxies ($N = 344$; i.e. excluding asymmetric galaxies, contaminated images, and bad fits). Here, we plot the difference in BIC$_{\rm res}$ between the selected 'best fit' and the next simplest (lower k) valid model, relative to the uncertainty in that ΔBIC$_{\rm res}$. A green dashed line is included to indicate the $3\sigma_{\rm res}$ limit, below which a model would not be chosen over a simpler alternative. This plot is comparable with fig. B1 in Paper I, which plots ΔBIC$_{\rm res}$ for Sérsic+ disc and Sérsic-only models.

While a number of galaxy models cluster close to the selection limit, only ∼20 per cent of models exhibit an improvement of less than $5\sigma_{\rm res}$ when compared to a less complex model. The results of this work are thus insensitive to slight changes to the ΔBIC$_{\rm res}$ selection limit. Therefore, model selection based on a BIC test is robust for comparing multicomponent galaxy models.

A more detailed discussion of the BIC test for model selection is available in Paper I and Head (2014). These works provide further details on the formulation of equation (1), and include comparison of BIC-selected models with by-eye selection, and F-test model selection.

APPENDIX C: FITTING RESULTS CATALOGUE

Multicomponent i-band fitting results for the extended Coma Cluster sample ($N = 631$, including blue galaxies) are presented in Table C1 (column descriptions in Table C2). The structural parameters of the best-fitting model (indicated by 'Model') are presented for each galaxy, including values for the total luminosity and combined half-light radius.[7]

[7] This value is an upper bound to the true value based on the assumption that major axes of all model components are aligned on the sky.

Table C1. The structural and photometric parameters of multicomponent models fits (*i* band) for the entire galaxy sample. The column headings are described in Table C2. This table displays the first 15 data rows only; the complete version will be made available online.

ObjID PA_1 q_3	RA $C0_1$ PA_3	Dec. $M_{i,2}$ $R_{\mathrm{e,out}}$	z $R_{\mathrm{e},2}$ r_{brk}	$M_{i,\mathrm{tot}}$ n_2 C_1/T	$R_{\mathrm{e,tot}}$ q_2 C_2/T	$M_{i,1}$ PA_2 C_3/T	$R_{\mathrm{e},1}$ $M_{i,3}$ Model	n_1 $R_{\mathrm{e},3}$ Profile	q_1 n_3 Flag
1237665427552927881 118.556 999.0	194.875 0.0 999.0	28.7 −18.16 999.0	0.024 1.237 999.0	−18.364 1.0 0.171	1.1 0.826 0.829	−16.449 121.312 0.0	0.233 999.0 BD	6.96 999.0 3	0.8 999.0 0
1237665427552927902 97.153 0.824	195.926 0.0 79.766	28.906 −17.089 2.417	0.022 4.686 5.914	−19.763 0.128 0.139	502.0 0.769 0.085	−17.618 13.057 0.776	0.53 −19.488 BSDd	1.008 7.865 312	0.955 1.0 1
1237665427552993436 167.424 0.706	195.018 0.0 21.469	28.603 −18.758 999.0	0.023 2.917 999.0	−20.068 0.374 0.206	3.73 0.838 0.299	−18.354 8.609 0.495	1.221 −19.303 BSS	1.927 6.369 311	0.68 0.486 0
1237665427552993478 29.906 999.0	195.095 0.0 999.0	28.574 −18.324 999.0	0.022 4.354 999.0	−19.109 0.44 0.515	3.3 0.858 0.485	−18.388 111.1 0.0	2.162 999.0 BS	2.124 999.0 3	0.659 999.0 0
1237665427553124587 137.698 999.0	195.449 0.0 999.0	28.66 999.0 999.0	0.029 999.0 999.0	−18.288 999.0 1.0	2.143 999.0 0.0	−18.288 999.0 0.0	2.143 999.0 S	1.649 999.0 5	0.723 999.0 0

Table C2. This table describes the column headings for Table C1, presenting multicomponent fitting results in the *i* band. Best-fitting model types are described in Section 3, (inner component/outer component) Allen et al. (2006) types are described in Section 3, and fitting flags are described in Table C3.

Column name	Description
ObjID	SDSS DR8 object ID
RA	Object right ascension [deg]
Dec.	Object declination [deg]
z	Object SDSS redshift
$M_{i,\mathrm{tot}}$	Total rest-frame magnitude
$R_{\mathrm{e,tot}}$	Upper limit total half-light radius [kpc]
$M_{i,1}$	Component 1 rest-frame magnitude
$R_{\mathrm{e},1}$	Component 1 half-light radius [kpc]
n_1	Component 1 Sérsic index
q_1	Component 1 axis ratio (b/a)
PA_1	Component 1 position angle [deg]
$C0_1$	Component 1 boxiness
$M_{i,2}$	Component 2 rest-frame magnitude
$R_{\mathrm{e},2}$	Component 2 half-light radius [kpc]
n_2	Component 2 Sérsic index
q_2	Component 2 axis ratio (b/a)
PA_2	Component 2 position angle [deg]
$M_{i,3}$	Component 3 rest-frame magnitude
$R_{\mathrm{e},3}$	Component 3 half-light radius [kpc]
n_3	Component 3 Sérsic index
q_3	Component 3 axis ratio (b/a)
PA_3	Component 3 position angle [deg]
$R_{\mathrm{e,out}}$	Outer disc half-light radius [kpc]
r_{brk}	Disc break radius [kpc]
C_1/T	Component 1 light fraction
C_2/T	Component 2 light fraction
C_3/T	Component 3 light fraction
Model	Best-fitting model
Profile	(B/D) Allen et al. (2006) type
Flag	Fitting flag

Table C3. This table describes the multicomponent fitting flag codes, as used in Table C1.

Flag code	Description	Condition
0	Normal fit	N/A
1	Bad fit (removed)	See Fig. B4
2	High chi-squared	$1.1 < \chi^2_\nu < 1.2$
3	Low component fraction	Any $0.05 < C/T < 0.10$
4	Small break radius	$r_{\mathrm{brk}} < 5$ arcsec

A value of 999.0 indicates a parameter is not present in the relevant best-fitting model (e.g. disc break radius in an unbroken *BD* galaxy). Fit quality flags ('Flag') are explained in Table C3.

This paper has been typeset from a TEX/LATEX file prepared by the author.